Scaling Up a Quantum Register of Dark Electronic Spins in Diamond

By

Alexander Ungar

S.B., University of California, Berkeley (2020)

Submitted to the Department of Electrical Engineering and Computer Science in Partial Fulfillment of the Requirements for the Degree of

Master of Science

at the

MASSACHUSETTS INSTITUTE OF TECHNOLOGY

SEPTEMBER 2023

Authored by: Alexander Ungar
Department of Electrical Engineering and Computer Science
August 29, 2023

Certified by: Paola Cappellaro
Ford Professor of Engineering
Professor of Physics
Thesis Supervisor

Accepted by: Leslie A. Kolodziejski
Professor of Electrical Engineering and Computer Science
Chair, Department Committee on Graduate Students

Scaling Up a Quantum Register of Dark Electronic Spins in Diamond

by

Alexander Ungar

Submitted to the Department of Electrical Engineering and Computer Science
on August 29, 2023, in partial fulfillment of the
requirements for the degree of
Master of Science in Electrical Engineering and Computer Science

Abstract

Electronic spin defects in the environment of an optically-active spin can be used to increase the size and hence the performance of solid-state quantum registers, especially for applications in quantum metrology and quantum communication. Previous works on multi-qubit electronic-spin registers in the environment of a Nitrogen-Vacancy (NV) center in diamond have only included spins directly coupled to the NV. As this direct coupling is limited by the spin coherence time, it significantly restricts the register's maximum attainable size. To address this problem, this thesis presents a scalable approach to map out and control a network of interacting environmental spins. We use this approach to characterize a spin network beyond the direct-coupling limit and exploit a weakly-coupled probe spin to mediate the transfer of spin polarization between the central NV and an environmental spin that is not directly coupled to it. We then demonstrate both detection and coherent control of this electronic spin outside the coherence limit of the central NV. Our work paves the way for engineering larger quantum spin registers with the potential to advance nanoscale sensing, enable correlated noise spectroscopy for error correction, and facilitate the realization of spin-chain quantum wires for quantum communication.

Thesis Supervisor: Paola Cappellaro
Title: Ford Professor of Engineering and Professor of Physics

Acknowledgments

While I am not even halfway through the PhD program, the first couple of years have already been quite a journey. I am extremely grateful to have ended up where I am today, despite the rocky beginning.

First, I would like to thank my advisor Paola for setting me up best for success in graduate school, and giving me another shot to join the group. She has encouraged me to pursue my interests in the lab and given me the space to learn at my own pace, while always helping me work through the challenging phases of my research. I am looking forward to more productive years under her guidance and to continuing the fun times in the group.

I would like to thank my academic advisor and department administrator Leslie as she has worked with me every step of the way during my last minute move to MIT and the transition between groups. Despite her many responsibilities she is always available to meet when necessary and I really value her advice as I navigate through graduate school.

Thank you to the QEG team for being so enthusiastic about each others projects and for creating a great learning environment. Being able to connect with each of you– whether it be over coffee/lunch, out on the sail boats, or on the volleyball courts– has made my first two years very enjoyable.

Lastly, I would like to thank my parents for making everything possible and being my number one fans throughout this journey. Your support for and faith in the path I have chosen truly means the world.

I would like to dedicate this thesis to my Grandpa Don who happens to be turning ninety seven on the day this is submitted. Through our frequent conversations over the phone, your words of wisdom and advice which you continue to share always help me to see things with a clear perspective. Happy Birthday Grandpa!

Contents

1 Introduction **17**

2 Background **21**

2.1 The NV center 22

2.2 Creation and discovery of environmental dark spins 23

2.3 Experimental apparatus 26

2.3.1 Optical setup 26

2.3.2 Electronics setup 28

2.3.3 Additional hardware 30

2.4 The Hamiltonian for the spin network 31

2.5 Control sequences 33

2.5.1 Spin-echo double resonance (SEDOR) 33

2.5.2 Hartmann-Hahn Cross Polarization (HHCP) 36

2.5.3 The measurement sequence 39

3 Spin network characterization **43**

3.1 System identification with spin-echo double resonance (SEDOR) . . . 43

3.1.1 Detection of first-layer spins X_1 and X_2 44

3.1.2 Detection of a second-layer spin Y 48

3.1.3 Constructing the graph structure 52

3.2 Nuclear spin identification with ENDOR 58

4 Achieving universal control of a second-layer spin **63**

4.1 Initialization of the spin chain 64
4.2 Unitary control and detection of Y 65
4.3 Scaling the register to larger networks of spins 68

5 Conclusion and Outlook **71**

A **73**

A.1 Data Analysis 73

List of Figures

2-1 (a) The defect structure of the NV center shown within the diamond lattice unit cell. Depicted here is one of four possible molecular orientations, defined by the nitrogen-vacancy bond direction. (b) Electronic energy level structure of the NV center, showing the triplet ground and excited state manifolds, as well as the singlet metastable state involved in the spin polarization process. The Δ represents the ground state zero-field splitting (image credit: Paola Cappellaro). 22

2-2 (a) Ion implantation of nitrogen-15 to create single NV centers strongly coupled to environmental dark spins. The ion energy and dose used was 14 keV and 1x10^{13} cm^{-2}, respectively. Previous SRIM results estimate a mean depth of $\sim$ 20 nm, with a straggle of $\sim$ 6 nm [11]. The inter-defect spacing per aperture is estimated to be $\sim$ 17 nm (11 kHz). Image adapted from [47]. (b) Implantation mask layout with nano-apertures, and confocal NV fluorescence image of the highlighted region containing a 5X5 array of implantation spots. The single NV we use for our experiments is located in the red dashed square on the confocal image. Other spots in the image correspond to multiple NVs per spot with aligned (brighter) or misaligned (dimmer) molecular orientations with respect to the polarization of the incident light. . . 25

2-3 The optical setup used to image single NVs. (a) Excitation stage, including the laser and double-pass acousto-optic modulator (AOM) (b) Confocal microscope stage, consisting of a 100X, 1.3 NA objective (c) Single photon detector stage. 27

2-4 (a) The microwave electronics setup used to apply coherent microwave pulses to control the electronic spins. This block diagram includes the microwave components for a single channel on the PCB. Our setup consists of two independent microwave circuits, one to drive the NV electronic spin (qubit splitting $\sim$ 1.85 GHz) and one to drive the environmental dark spins (qubit splitting $\sim$ 1 GHz). (b) The digital electronics setup to communicate with the AWG and data acquisition module. 29

2-5 NV spin contrast $\langle\sigma_z^{\mathrm{NV}}\rangle$ mapping to the dark spin contrast $\langle\sigma_z^{\mathrm{X}}\rangle$ (where X is the label for a first-layer dark spin to be identified in Chapter 3). Both X hyperfine transitions are driven to address 100% of the electronic spin population for X. 41

3-1 The SEDOR(NV,X) experimental sequence is used to identify first-layer spins in the environment of a central NV. The NV is initialized and read out with a green laser pulse, and the m.w. sequence is composed of a spin-echo on the probe spin (NV) with a recoupling π-pulse on the target spin (X). Darker (lighter) shading indicates a pulse along y (x). The recoupling pulse frequency (ω) can be swept for SEDOR-ESR(NV,X) to measure ω_0^{X}, and the recoupling time (T) can be swept for SEDOR-Ramsey(NV,X) to measure $d^{\mathrm{NV,X}}$. 45

3-2 The SEDOR-ESR(NV,X) experimental data show the resonance frequencies and hyperfine splittings of the first-layer spins labeled X_1 (A = 26.5(6) MHz) and X_2 (A = 3.0(5) MHz), and confirm both belong to electronic spin-1/2 and nuclear spin-1/2 defects. The x-axis corresponds to the intermediate frequency in our mixer circuit, with an LO frequency of $\sim$960 MHz. Solid lines are Lorentzian fits to the data (details in Appendix A.1). The pulse sequence above consists of a spin-echo on the probing spin (NV) at fixed evolution time, and a recoupling π-pulse on the target spin (X_1, X_2) at a variable frequency. 46

3-3 (a) The SEDOR-Ramsey(NV,X) experimental data show coherent oscillations mediated by the dipolar coupling between the NV and X spins, and allow us to extract the coupling strengths to the first-layer spins, $d^{\mathrm{NV,X1}}$ and $d^{\mathrm{NV,X2}}$. Here we drive only one hyperfine transition for X, leading to a reduction in contrast by 50%. Also for reference we plot the spin-echo(NV) data, for which we extract the NV coherence time of $T_2^{\mathrm{NV}} = 50(10)\ \mu s$. The pulse sequence above consists of a spin-echo on the probing spin (NV) at swept recoupling time, and a recoupling π-pulse on resonance with the target spin (X_1,X_2). (b) The FFTs of the SEDOR-Ramsey(NV,X) signals reveal single dominant peaks in both spectra and confirm X_1 and X_2 are non-degenerate, with $d^{\mathrm{NV},X1} = 67(14)$ kHz and $d^{\mathrm{NV},X2} = 38(13)$ kHz. 47

3-4 The SEDOR(X,Y) experimental sequence is used to identify second-layer spins using X as a probe (where X can be either X_1 or X_2). X is initialized and read out via the NV using HHCP. HHCP consists of simultaneous spin-locking two dipolar-coupled spins at matched Rabi frequencies, and an iSWAP gate can be achieved by setting the spin-lock duration to $1/(2d)$, where d is the dipolar-coupling strength. A second-stage SEDOR sequence is applied between X and Y, where now an initialized X spin is the probe and can be used to characterize a nearby coupled dark spin, Y. The recoupling pulse frequency (ω) can be swept for SEDOR-ESR(X,Y) to measure ω_0^{Y}, and the recoupling time (T) can be swept for SEDOR-Ramsey(X,Y) to measure $d^{\mathrm{X,Y}}$. . 49

3-5 The SEDOR-ESR(X_1,Y) experiment uses X_1 as the probing spin to identify the second-layer spin Y. The experimental data show the resonance frequencies and hyperfine splitting of Y (A = 33.5(3) MHz), and confirm it is an electronic spin-1/2 and nuclear spin-1/2 defect. The y-axis scale $\langle\sigma_z^{\mathrm{X}}\rangle$ is normalized and shifted from the NV signal $\langle\sigma_z^{\mathrm{NV}}\rangle$ according to the mapping presented in Section 2.5.3. 50

3-6 (a) The SEDOR-Ramsey(X_1,Y) experiment uses X_1 as the probing spin to measure the coupling strength between X_1 and Y. The experimental data show coherent oscillations mediated by the dipolar interaction. Here we drive only one hyperfine transition for Y, leading to a reduction in contrast by 50%. (b) The FFT of the SEDOR-Ramsey(X_1,Y) data reveals a single dominant peak in the spectrum and confirms Y is non-degenerate, with $d^{X1,Y} = 20(4)$ kHz. 50

3-7 SEDOR experiments on the NV and X_1 spins at the Y resonance frequency, showing the NV and Y are not coupled and that Y can be characterized as a second-layer spin. The top plot is adapted from Figure 3-5 and shows the SEDOR-ESR(X_1,Y) resonance signal which locates ω_0^Y. The bottom plot shows the results of the SEDOR-ESR measurement on the NV performed at a recoupling time of T_2^{NV} (threshold for coupling to a first-layer spin), with no resonance signal at the Y frequency. The data is shifted to account for the decoherence of the NV during the spin-echo decay. 54

3-8 SEDOR experiment with X_2 as the probing spin to rule out its coupling to Y. The SEDOR-Ramsey(X_2,Y) experiment shown applies the recoupling pulse on resonance with the Y frequency as the interaction time is swept. The data together with the fitted exponential decay (details in Appendix A.1) rule out coherent oscillation with a single spin at the Y frequency. The outliers to the fit may be the result of X_2 control imperfections or several degenerate Y spins coupled to X_2 with different coupling strengths. We apply the same scaling for $\langle\sigma_z^{X2}\rangle$ to convert from $\langle\sigma_z^{NV}\rangle$ as we do for the X_1 signal. 55

3-9 SEDOR-ESR experiment with X_1 as the probing spin to rule out its coupling to X_2. The SEDOR-ESR(X_2,X_1) experiment is performed at $T = 20$ μs and $T = 40$ μs and compared with the X_2 resonance signal as detected through the NV (adapted from Figure 3-2 and displayed above). The lack of contrast in the X_1 signal at the X_2 frequency confirms the two first-layer spins are not coupled. 56

3-10 Illustration of the spin-graph structure as characterized using SEDOR for the system of four spins consisting of the central NV, and environmental dark spins X_1, X_2, and Y. To summarize, X_1 and X_2 are first-layer spins directly coupled to the NV and not coupled to each other. Y is a second-layer spin directly coupled to X_1 and not coupled to the NV. The NV, X_1, and Y spins form a chain since Y and X_2 are not coupled. 57

3-11 ENDOR experiment on the X_2 defect with a 32 μs π-pulse calibrated for the nitrogen nuclear spin. The resonance frequency extracted from the fit at 1.42(2) MHz confirms the X_2 nuclear spin is nitrogen. . . . 60

3-12 Comparing the NV-nuclear spin Rabi measurement with the ENDOR-Rabi measurement on X_2. For ENDOR, the r.f. pulse is applied on resonance with the X_2 nitrogen nuclear spin transition. The Rabi frequencies extracted from the cosine fits are 15.8(5) kHz and 13.5(4) kHz for the NV and X_2 nuclear spins, respectively, further confirming X_2 is comprised of a nitrogen nuclear spin. 61

4-1 Quantum circuit and experimental data demonstrating polarization transfer between the NV and X spins via HHCP. The polarization of the NV, as measured by $\langle\sigma_z^{\mathrm{NV}}\rangle$, reaches a minimum near the iSWAP time of $1/(2d^{\mathrm{NV,X}})$, leaving X in a polarized state. The FFT spectrum characterizes the frequency of polarization transfer, which is consistent with the dipolar coupling strength as measured in SEDOR (Figure 3-3). The I and M blocks in the quantum circuit represent laser pulses to initialize and measure the NV. 64

4-2 Quantum circuit and experimental data demonstrating polarization transfer between the X and Y dark spins via HHCP. The polarization of X, as measured by $\langle\sigma_z^{\mathrm{X}}\rangle$, reaches a minimum near the iSWAP time of $1/(2d^{\mathrm{X,Y}})$, leaving Y in a polarized state, and confirms the successful implementation of cascaded polarization transfer to initialize Y. The signal is normalized as for SEDOR-X, and an additional offset is added such that the maximum fit value equals 1 (see Appendix A.1 for further details). The FFT spectrum shows the frequency of polarization exchange is at the expected dipolar coupling strength, $d^{\mathrm{X,Y}}$. The iS blocks in the quantum circuit represent iSWAP gates between 2 spins implemented using HHCP set to a spin-lock duration of $1/(2d)$. . . . 66

4-3 Achieving unitary control of Y by detecting Rabi oscillations. Y is initialized and read out by applying sequential iSWAP gates along the chain, using the HHCP(NV,X) and HHCP(X,Y) gates calibrated from the signals in Figures 4-1 and 4-2. We apply a microwave (m.w.) pulse of swept duration on resonance with the Y electronic spin transition to drive Rabi-oscillations. The y-axis scale is the NV contrast, and creates a mapping of the Y spin state for readout. The R(θ) block in the quantum circuit represents a pulse of length $L = \theta/\Omega_0^{\mathrm{Y}}$ where $\Omega_0^{\mathrm{Y}} = 0.5$ MHz. 67

4-4 Measuring the T_1 decay time of Y under laser illumination, which shows stability over a long enough time scale (a few times the typical iSWAP gate length) to enable repetitive readout and an additional memory qubit in the register. 68

Chapter 1

Introduction

Optically-active solid-state spin defects with individual control are promising building blocks for quantum information processing [3]. Notable among defects in diamond, the Nitrogen-Vacancy (NV) center is a leading candidate for applications in quantum sensing [14], while the silicon-vacancy center is a key prospect for realizing efficient quantum networks [46]. Still, engineering a quantum register consisting of individually controllable environmental spins surrounding a central optically-active spin enables more powerful and interesting applications. For instance, a quantum register of nuclear spins is ideal for storing and processing quantum information given its weak coupling to the environment. Such a nuclear-spin register has thus been used to demonstrate enhanced quantum memory with record lifetimes [1, 5], quantum error correction [51], and quantum simulation [40]. On the other hand, a register consisting of electronic spins, which feature stronger coupling to external fields and other spins, can enable new and complementary applications. In the areas of quantum sensing and quantum device characterization, such an electronic-spin register can be used for correlated noise spectroscopy and error characterization [42, 57, 54, 50], as well as high-resolution sensing in spatial and frequency domains [9], even surpassing the standard quantum limit in sensing [6, 22, 11].

Until now, electronic-spin registers comprising an NV center electronic spin (referred to herein as NV) and optically-inactive (dark) spins in its environment have been limited in size, as they only include spins which are directly coupled to the cen-

tral NV via the magnetic-dipolar interaction [15, 10, 48, 41, 29]. Similarly, registers consisting of multiple NVs have been limited in size to pairs of NVs that are directly coupled [17, 38, 26, 30]. In the case of dark spin registers, the coherence volume, which we define as the volume encompassing all of the spins that can be coherently controlled, has been limited by the coherence time of the central NV. We refer to the spins within this coherence-time limit as first-layer spins. To pertain to this first layer, the dipolar coupling strength between the first-layer spins and the central NV, denoted as $d(\vec{r})$, must satisfy the condition $d(\vec{r}) \gtrsim 1/T_2$, where T_2 is the NV's coherence time. If spins beyond this first layer could be accessed, the coherence volume of spin registers could be scaled up beyond the NV coherence-time limit.

A promising approach to surpass the coherence-time limit is utilizing a coherent first-layer spin to identify and subsequently control a second-layer spin not directly coupled to the central spin. Accessing such larger spin registers would enable preparing correlated states of electron spins to improve metrological performance in magnetic sensing applications, ultimately achieving a sensitivity scaling with $\sqrt{n}$ for an n-spin register [20, 10]. Furthermore, controlling spins beyond the first layer would facilitate searching for novel paramagnetic defects [11], gaining further insights into surface spin dynamics [18], and improving imaging of spin-labeled molecules on the surface of diamond [44].

In this thesis, we demonstrate how to extend the coherence volume of a network of dark spins surrounding a central NV beyond the coherence-time limit of the NV. We first develop novel control protocols to identify three unknown dark spins surrounding the NV up to the second layer. We then subsequently map out the interaction graph structure of the four-spin network consisting of the NV and the dark spins referred to as X_1, X_2, and Y. This approach exploits a mediator first-layer spin (X_1) to identify a second-layer spin (Y) using spin-echo double resonance (SEDOR) measurements [13]. We find that the three-spin system (NV, X_1, Y) forms a chain where Y is located outside the coherence limit of the central NV. We also find that X_1, X_2, and Y are formed from distinct defects, allowing for selective microwave (m.w.) control. Furthermore, we demonstrate how universal single-qubit control can be extended to

this second-layer spin. We initialize and read out the state of the Y spin by performing polarization transfer across the spin-chain using Hartmann-Hahn Cross Polarization (HHCP) [21]. We then successfully implement coherent control of the Y spin by driving and measuring Rabi oscillations. [1]

Our results demonstrate successful application of the building blocks necessary for realizing single-spin sensing over a greater volume with distant reporter spins [49]. Our approach can also be extended to identify and control environmental spins in higher layers by recursively applying the SEDOR and HHCP control blocks. In this way, an electronic-spin register can be scaled up into a larger network of individually addressable spins without being limited by the coherence time of the central NV. Assembling this network might also lead to the discovery of as-yet-unknown electron-nuclear spin defects with interesting features [11].

This thesis is organized into the following chapters. In Chapter 2 we introduce some basic background on the optically active NV center in diamond which serves as our central qubit for the register (Section 2.1). We also discuss the implantation process for engineering single NV centers in diamond, which also leads to the formation of environmental dark spin defects interacting with the NV centers (Section 2.2). Following this, we review how our experimental setup is used to image single NV centers and control the electronic spins of paramagnetic defects via microwave driving (Section 2.3). We then discuss how to characterize the spin Hamiltonian for an arbitrary network of dark spins surrounding a central NV center, which can be harnessed as qubits in a quantum register (Section 2.4). This is followed by analytical density matrix calculations to analyze the control sequences used to initialize and detect dark spins with Hartmann-Hahn Polarization (HHCP) and spin-echo double resonance (SEDOR), respectively (Section 2.5). In Chapter 3 we introduce and apply our identification protocol using SEDOR and HHCP to characterize the spin Hamiltonian of a network of dark spins surrounding a single NV center (Section 3.1). We then seek to identify the nuclear spin species of one of these novel defects using electron-nuclear

[1] This demonstration of control beyond the coherence limit of the NV spin is highlighted in our recently submitted paper currently on arXiv [53]

double resonance (ENDOR) techniques (Section 3.2). In Chapter 4 we demonstrate universal control of the second-layer spin in the network through initialization of the spin-chain (Section 4.1) and detection of Rabi oscillations (Section 4.2). Finally, we discuss the practical limits to scaling electronic spin registers to higher layers using our protocol (Section 4.3).

Chapter 2

Background

Diamond is host to many different types of point defects in the lattice which can result from vacancies, substitutional impurities, or atom interstitials (or any combination of the three) [8]. Defects involving nitrogen impurities are the most common in natural diamond samples, and can also be introduced into synthetic samples by tailoring the growth process or using ion implantation [37]. For our work, we are interested in paramagnetic defects which feature one or more electrons that can be manipulated by electromagnetic radiation (microwaves or laser light) and where the spin degree of freedom can be harnessed as a qubit. Our work will focus on controlling the Nitrogen-Vacancy (NV) center as a central qubit which will allow us to characterize and control nearby unidentified defects formed during the implantation process.

This chapter presents the relevant background material related to our experimental system, including the physical properties of the NV center (Section 2.1), the sample preparation leading to the creation of novel environmental defects (Section 2.2), and the control hardware used in the setup (Section 2.3). We will then introduce the spin network model through the Hamiltonian which connects the NV center and these environmental defects (Section 2.4). Finally, we will review the basic quantum protocols used to probe and control each spin in the network (Section 2.5).

2.1 The NV center

The NV center is the leading candidate for many solid-state quantum information processing tasks due to its spin-dependent optical transitions and long coherence time at room temperature [3]. These properties allow for the spin state to be polarized via laser illumination and then coherently manipulated via resonant microwave (m.w.) pulses. Furthermore, the fluorescence intensity during laser illumination allows for distinguishable measurement of the spin polarization.

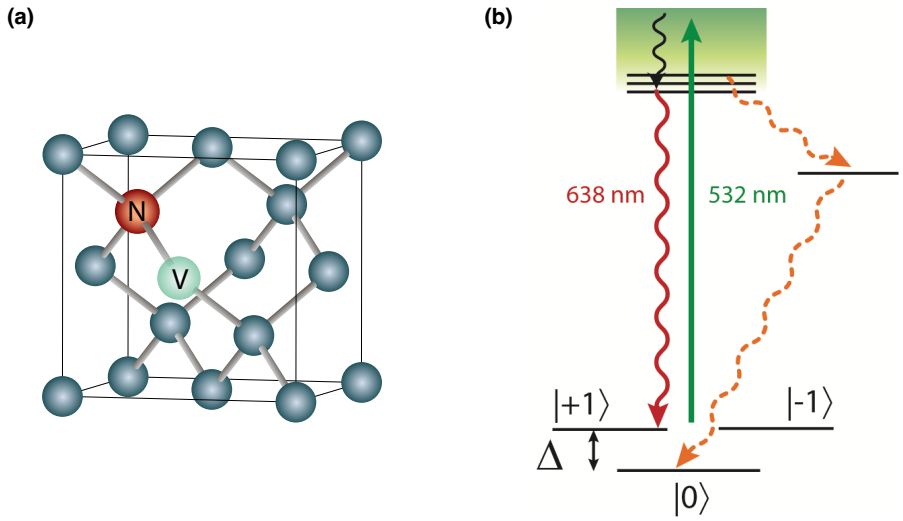

Figure 2-1: (a) The defect structure of the NV center shown within the diamond lattice unit cell. Depicted here is one of four possible molecular orientations, defined by the nitrogen-vacancy bond direction. (b) Electronic energy level structure of the NV center, showing the triplet ground and excited state manifolds, as well as the singlet metastable state involved in the spin polarization process. The Δ represents the ground state zero-field splitting (image credit: Paola Cappellaro).

The NV center in diamond is formed by a substitutional nitrogen atom and an adjacent vacancy in the lattice, as shown in Figure 2-1(a). Due to the interactions between the valence electrons from the nitrogen and nearby carbons, the NV center is an electronic spin-1 defect, featuring the electronic energy level structure illustrated in Figure 2-1(b). The electronic ground state is a spin triplet, consisting of the $m_S = 0$ and $m_S = \pm 1$ spin substates. The $m_S = \pm 1$ levels are shifted from the $m_S = 0$ level by the zero-field splitting energy of 2.87 GHz. In the presence of an external

magnetic field, the $m_S = \pm 1$ levels are non-degenerate and the splitting between two adjacent levels in this triplet manifold forms an effective two-level system. For our experiments, the two-level system consisting of the $m_S = 0$ and $m_S = -1$ states form the NV spin qubit which we control through microwave driving. Using an external magnetic field of approximately 360 G aligned with the molecular axis of the NV center, the energy splitting of the qubit is approximately 1.85 GHz.

The NV center electronic spin can be optically pumped via illumination with a green laser pulse (532 nm), leading to the polarization of the $m_S = 0$ level in the ground state. Absorption of green photons will transfer population in the ground electronic state to the excited electronic state while conserving spin. The optical pumping mechanism results from a preferential decay pathway from the $m_S = \pm 1$ levels in the excited state through the metastable state [52]. Since relaxation through the metastable state is non-radiative, the fluorescence is higher for the $m_S = 0$ state, allowing for spin-state selective optical readout. These properties, along with a coherence time of up to several milliseconds at room temperature [4], make the NV center electronic spin ideal to serve as the central qubit in a quantum register.

2.2 Creation and discovery of environmental dark spins

The requirements for a useful quantum register of electronic spins are individual control of each spin and connectivity between all spins (direct or indirect coupling as determined by the graph structure). Spins can interact through the mutual magnetic-dipolar interaction, where the coupling strength, d, scales inversely with the separation distance ($d \propto 1/r^3$). The finite coherence time of electronic spins in diamond sets a lower bound on the coupling strength, translating into a maximum separation distance between spins which is around 10-20 nm. Given that the diffraction limited laser spot is on the order of a few hundred nanometers, constructing a quantum register consisting of multiple NVs is difficult. Specifically, optically addressing one NV will affect the state of the other NVs in the register. While individual spin state

readout on pairs of NVs has been achieved using local spin operations and repetitive readout [17], as well as with superresolution optical imaging [27], it remains an open challenge to implement this on larger systems of coupled NVs. Thus, a more practical quantum register should consist of a single NV center electronic spin connected to environmental spins which are stable under optical illumination. Such environmental spin defects are referred to as dark spins, and they do not feature any spin-dependent optical transitions at or near the wavelengths used for NV optical control.

We use ion implantation through nano-apertures (with a diameter of approximately 30 nm) to create an array of single NV centers. The pitch of the array is 1 μm which allows for independent laser illumination for each implantation spot, where the diffraction limited spot size of our laser is $\sim$ 500 nm (see Section 2.3 for further details). We implant nitrogren-15 into an isotopically-enriched 12C diamond sample though a lithographically fabricated mask. The implantation energy and concentration were chosen to produce on average a single NV center per spot within $\sim$ 20 nm from the diamond surface (Figure 2-2). It was ultimately discovered by a previous student that the majority of implantation spots contain 2 NVs. However, we are able to locate one spot in particular that contains a single NV strongly coupled to several dark spins. We select this NV and its environmental spins to serve as our experimental system for the following work presented in Chapters 3 and 4.

Two possible ways in which defects could form in the diamond lattice are from the implanted nitrogen ions or from diffusion of other atoms during crystal synthesis or sample preparation steps (e.g the lithography process). However, the majority of the defects formed are derived from nitrogen since the implantation of nitrogen ions into the lattice has an N to NV conversion efficiency of only around 10% [36]. The simplest and most abundant defect in diamond is the P1 center, which consists of a substitutional nitrogen atom in the place of a carbon atom [39]. The neutral charge state of the defect is paramagnetic, and relative to the NV center features negligible absorption under green laser illumination (the measured absorption spectra shows a threshold below 270 nm [24]). Thus, the P1 center is one type of dark electronic spin defect in diamond and is featured in many experimental studies with NV centers

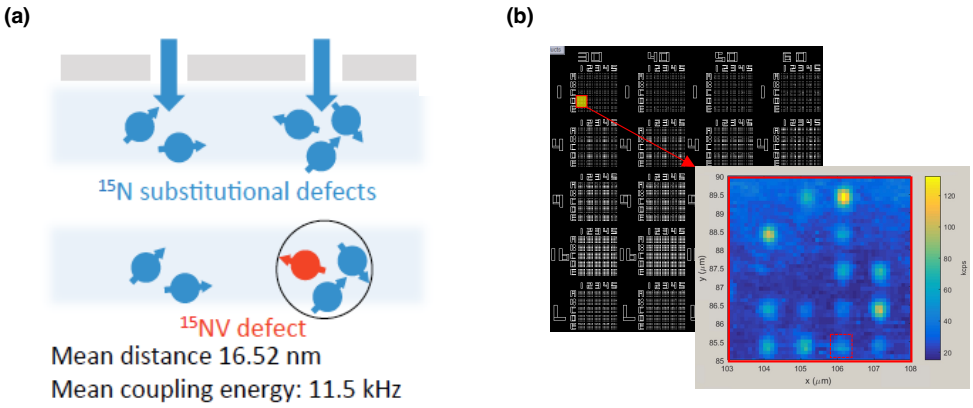

Figure 2-2: (a) Ion implantation of nitrogen-15 to create single NV centers strongly coupled to environmental dark spins. The ion energy and dose used was 14 keV and 1x10^{13} cm^{-2}, respectively. Previous SRIM results estimate a mean depth of $\sim$ 20 nm, with a straggle of $\sim$ 6 nm [11]. The inter-defect spacing per aperture is estimated to be $\sim$ 17 nm (11 kHz). Image adapted from [47]. (b) Implantation mask layout with nano-apertures, and confocal NV fluorescence image of the highlighted region containing a 5X5 array of implantation spots. The single NV we use for our experiments is located in the red dashed square on the confocal image. Other spots in the image correspond to multiple NVs per spot with aligned (brighter) or misaligned (dimmer) molecular orientations with respect to the polarization of the incident light.

[13, 15, 41, 12]. The recent state-of-the-art demonstration constructing an electronic spin register around a central NV used P1 centers as the environmental dark spins [15]. However, by using identical P1 defects, the total number of spectrally distinguishable spins is limited by the number of hyperfine and Jahn-Teller states intrinsic to the P1 defect [39]. An alternative approach to constructing larger spin networks of dark spins is to rely on distinct paramagnetic defect types which interact with each other and the central NV.

Previous work on our experimental system identified two novel and distinct dark spin defects, labelled X_1 and X_2, which are coupled to a single NV center [11]. A spin-echo double resonance (SEDOR) microwave control sequence was used to locate and characterize these two defects. The defects' resonance frequencies and coupling strengths were measured as a function of the external magnetic field orientation and strength. The hyperfine tensor components were extracted from these measurements, and it was also concluded the defects feature an electronic and nuclear spin-1/2 energy level structure. These two defects will be part of the spin-network which is charac-

terized in detail in Chapter 3. We refer to these spins as first-layer spins since they are directly coupled to the central NV electronic spin. They can be used to probe for new spins outside the coherence volume of the NV. In Chapter 4 we show how X_1 can mediate the transfer of spin polarization to a newly identified and distinct defect in the second-layer, enabling universal control of spins outside the NV coherence limit.

2.3 Experimental apparatus

2.3.1 Optical setup

The optical setup used to image and control single NVs consists of a home-built confocal microscope with a green laser for optical illumination (Figure 2-3). The optical setup can be divided into three stages, as indicated by the dashed outlines in the figure. The first stage includes the laser output (5 W Lighthouse Photonics Sprout diode pumped 532 nm laser) and the acousto-optic modulator (AOM) (Intraaction Corp AFM-80) to pulse the laser on and off with rise and fall times on the order of a few nanoseconds. The optics around the AOM are arranged in a double-pass configuration. This configuration allows for the 1^{st} order diffracted light of the input beam to be redirected back through the AOM. The second-pass beam's negative 1^{st} order output then propagates along the same direction as the original input beam. To separate the output light from the input light, the polarization of the output is rotated 90 degrees from the input by passing twice through a quarter-wave plate and is then reflected by a polarizing beam-splitter (PBS). By using the double pass configuration we are able to increase the extinction ratio between the on and off light intensities, and thus minimize the light illuminating the NV center when the AOM is gated off. We improve the extinction ratio further by using a fiber collimator which couples the mode-matched output light into an optical fiber and is routed into the confocal microscope stage of the setup.

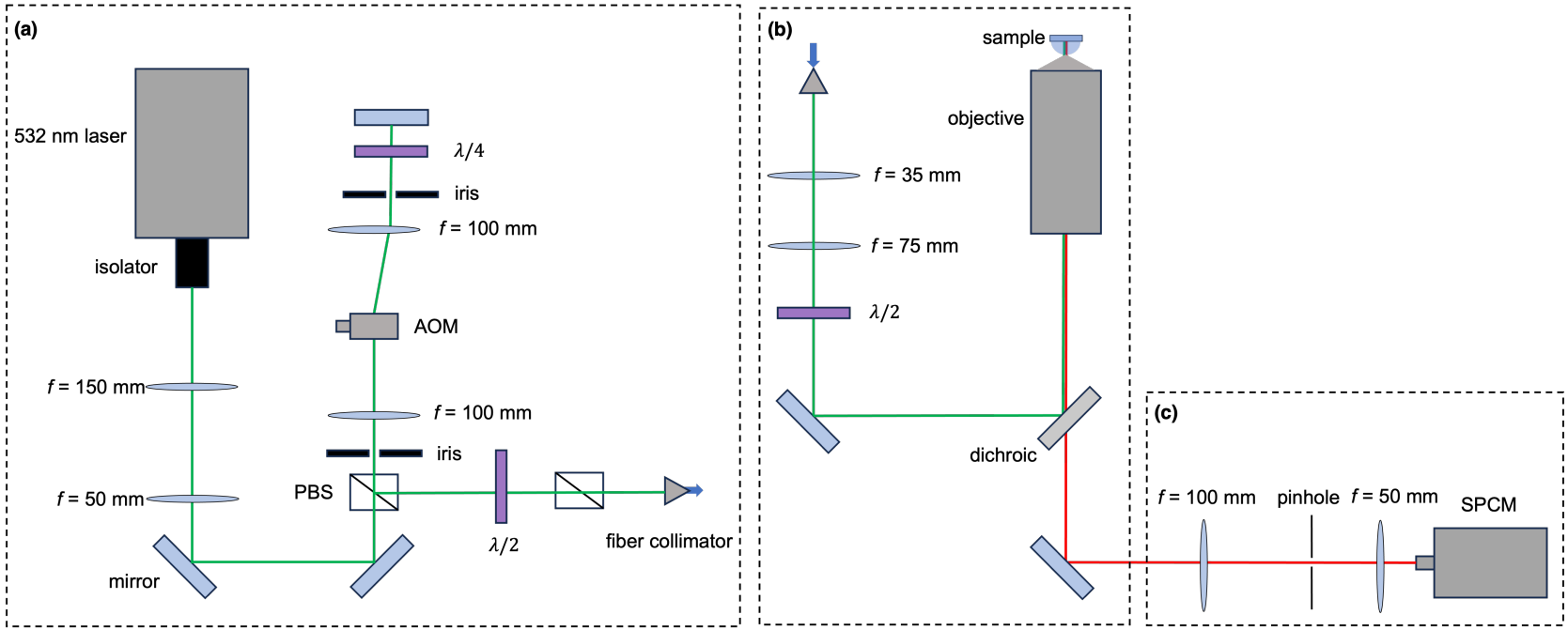

Figure 2-3: The optical setup used to image single NVs. (a) Excitation stage, including the laser and double-pass acousto-optic modulator (AOM) (b) Confocal microscope stage, consisting of a 100X, 1.3 NA objective (c) Single photon detector stage.

For the confocal microscope, we use a Nikon Plan Fluor 100X immersion oil objective with a numerical aperture of 1.3. The half-wave plate before the entrance of the objective tunes the polarization to increase optical absorption for a specific NV molecular orientation. The fluorescence from a single NV can be treated as a uniform spherical source of radiation which is collected within a solid angle determined by the numerical aperture. With illumination at 532 nm, which is higher in energy than the zero-phonon line at 638 nm, we excite a transition in the phonon-sideband. The subsequent emission back to the ground state occurs at wavelengths ranging from $\sim$ 650-800 nm at room temperature [34]. The fluorescence light propagates along the path of the green light and is then separated by a dichroic mirror and focused by a lens. For our setup, the lens focal length is 100 mm and the effective focal length of the objective is 2 mm, magnifying the diffraction limited emission spot at the source of $\sim$ 500 nm to an image spot size of 25 μm. A pinhole is used to filter out the light emitted from different depths in the sample, and hence is optimal to image a single layer of NVs at a specific depth. The fluorescence is collimated by another lens and collected by an avalanche photodiode (Perkin Elmer SPCM-AQRH).

2.3.2 Electronics setup

The layout of the microwave electronics setup can be seen in Figure 2-4(a). We generate microwave pulses for electronic spin driving using an Arbitrary Waveform Generator (Tektronix AWG 5014C). For each analog channel, we output two waveforms with a 90 degree phase offset for the IQ modulation, and a digital TTL output gated when the pulses are on to control the MW switches. We use two of the analog channels in order to independently drive near the two relevant transition frequencies for our spin system. The NV electronic spin has an additional zero field splitting term in its spin Hamiltonian (Section 2.4), while the dark spin transition is near the free electron Larmor frequency, making the two transitions offset by approximately 1 GHz at our field strength of 360 G. Thus we have two separate but identical microwave circuits to achieve independent and simultaneous driving at the NV and dark spin frequencies.

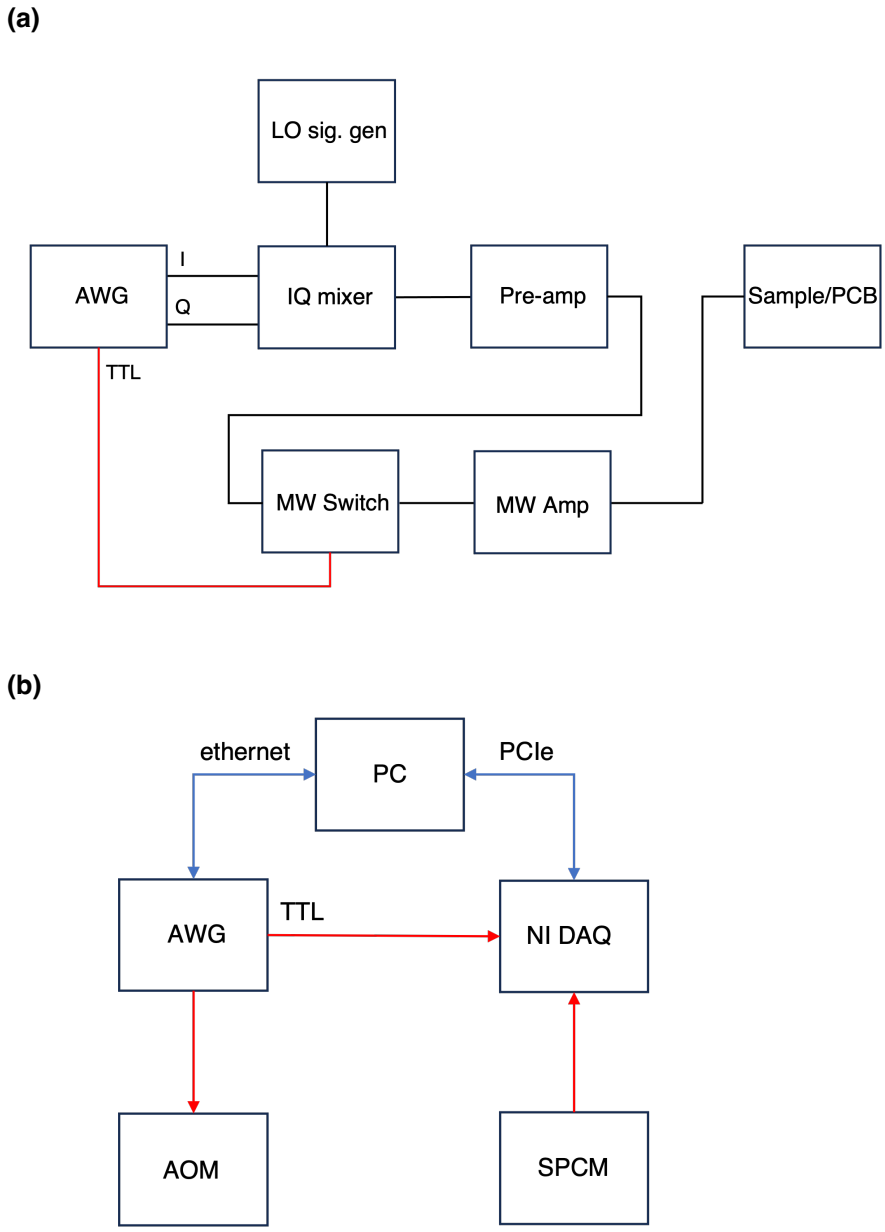

Figure 2-4: (a) The microwave electronics setup used to apply coherent microwave pulses to control the electronic spins. This block diagram includes the microwave components for a single channel on the PCB. Our setup consists of two independent microwave circuits, one to drive the NV electronic spin (qubit splitting $\sim$ 1.85 GHz) and one to drive the environmental dark spins (qubit splitting $\sim$ 1 GHz). (b) The digital electronics setup to communicate with the AWG and data acquisition module.

Given that the sampling rate of the AWG is limited to 1 Gs/s, we generate the microwave pulses at a carrier frequency between 40-100 MHz depending on the spin transition, and upconvert to the resonance frequency using an IQ mixer with the LO

signal outputted by an additional signal generator (SRS-SG384). Since the signal generator is always on during the experiment, we add a microwave switch gated by the TTL output of the AWG which helps to isolate the LO signal when the pulses are off (otherwise the LO can induce off-resonant driving). The upconverted signal is amplified by a high power microwave amplifier (Minicircuits ZHL-16W-43-S+ for the NV channel, ZHL-20W-13S+ for the dark spin channel). The microwave signals are delivered through a gold coplanar waveguide (CPW), which is fabricated on a glass coverslip and soldered onto a PCB board. The diamond is mounted on top of the CPW to maximize coupling to the microwave field. The other end of the PCB is connected to a 10 dB attenuator and 50 Ohm terminator. For the nuclear spin experiments in Section 3.2, we generate the r.f. pulses directly out of the AWG, which is amplified by a Minicricuits LZY-22+ power amplifier and connected to the output terminal on the NV CPW.

We run the control software for experiments through MATLAB, which contains packages to communicate with the AWG and data acquisition module (National Instruments PCI-6343 DAQ). The complete block diagram for the digital electronics setup can be seen in Figure 2-4(b). We use a TTL channel from the AWG to gate the AOM in order to pulse the laser on and off. The avalanche photodiode outputs a TTL pulse 15 ns wide corresponding to a count registered by a single photon (or a dark count). This is registered by the DAQ through a digital input, and then we collect the total counts within a desired time window by sending a TTL pulse from the AWG to the DAQ. This data is then sent to the PC and registered in the MATLAB control interface.

2.3.3 Additional hardware

To control the position of the sample and take scanning images of the NV array, the sample/PCB is mounted onto a piezo nanopositioner (Mad City Labs Three-axis Nano LP). The controller is interfaced with the analog output of the NI DAQ. To apply an external magnetic field we use a 1" cube neodynium magnet mounted on a three-axis translation stage, with motorized control along the [100] crystallographic

direction using a Zaber linear actuator.

One major challenge is keeping the temperature around the setup stable. Temperature drifts affect the magnetization (and hence the resonance frequency of the electronic spins) as well as the position of the diamond itself (leading to the NV drifting away from the focal plane of the microscope). To stabilize the temperature, we installed a home-built heater with closed-loop control using an arduino microcontroller. This keeps the setup stable to within 0.1 ° C, and allows us to increase the measurement duration before refocusing the laser on the NV and recalibratring the resonances.

2.4 The Hamiltonian for the spin network

The Hamiltonian for a network of dark spins surrounding a central NV takes the following form:

$$H = H_0^{\mathrm{NV}} + \sum_i \left(H_0^i + H_{\mathrm{int}}^{\mathrm{NV},i} \right) + \frac{1}{2} \sum_{i,j} H_{\mathrm{int}}^{j,i} \tag{2.1}$$

where i or j denotes the index for a single dark spin. For the NV with nitrogen-15, which is an electronic spin-1 and nuclear spin-1/2 defect, the secular Hamiltonian (neglecting energy non-conserving or spin-flip terms [31]) is:

$$H_0^{\mathrm{NV}} = D\tilde{S_z}^2 + \gamma_e B_0 \tilde{S}_z + A_{\parallel} \tilde{S}_z I_z, \tag{2.2}$$

where the external magnetic field direction is along the NV molecular axis (parallel to the z direction). Here D is the zero-field splitting term, γ_e is the gyromagnetic ratio, and $A_{\parallel}$ is the longitudinal hyperfine coupling term. Since we only drive the $\mathrm{m}_s = 0, -1$ states of the NV which form the spin-1/2 qubit, and the nuclear spin is nearly 100% polarized in one of the m_I substates at our field strength [38], we can trace out the nuclear spin and $m_s = +1$ subspaces. This allows us to rewrite the above Hamiltonian in terms of the spin-1/2 S_z operator (ignoring any components proportional to the identity operator): $H_0^{\mathrm{NV}} = \omega_0^{\mathrm{NV}} S_z$, where $\omega_0^{\mathrm{NV}} = D - \gamma_e B_0 + m_I A_{\parallel}$.

The dark spins discovered in the environment of our specific NV under study are

all electronic spin-1/2 and nuclear spin-1/2 defects (see Chapter 3 for the characterization). The secular Hamiltonian for the i^{th} dark spin is (assuming a uniaxial hyperfine tensor [45]):

$$H_0^i = \gamma_e B_0 S_z^i + A^i S_z^i I_z^i + B^i S_z^i I_x^i. \tag{2.3}$$

where A and B are components of the hyperfine tensor transformed from the dark spin molecular frame to the the NV molecular frame: $(R^{\text{NV},i})\text{Diag}[A_\perp^i, A_\perp^i, A_\parallel^i](R^{\text{NV},i})^T$. The dark spin qubit splitting in the m_I manifold is:

$$\omega_0^i = \gamma_e B_0 + m_I A_{\text{eff}}^i, \tag{2.4}$$

where $A_{\text{eff}}^i = \sqrt{(A^i)^2 + (B^i)^2}$. The interaction between spins arises from the magnetic-dipolar coupling. The secular interaction term between dark spins in the Hamiltonian is:

$$H_{\text{int}}^{i,j} = 2d^{i,j} S_z^i S_z^j, \tag{2.5}$$

and is expressed equivalently for $H_{\text{int}}^{\text{NV},i}$. Then the total spin Hamiltonian for the network is:

$$H = \omega_0^{\text{NV}} S_z + \sum_i \left(\omega_0^i S_z^i + 2d^{\text{NV},i} S_z S_z^i\right) + \sum_{i,j} d^{i,j} S_z^i S_z^j. \tag{2.6}$$

Note that all constants above are expressed in angular frequencies, where the factor of 2π is absorbed. The goal for the Hamiltonian identification for the spin network is to measure each term in the above expression within our experimental limits. Both the microwave control fidelity and the coupling strength between spins relative to the coherence time of the probing spins will play a role in limiting the size of the network that can be characterized. The primary goal of our experiments is to identify and control environmental spins in the network beyond the first layer. We refer to a dark spin i as a first-layer spin if $d^{\text{NV},i} > 1/T_2^{\text{NV}}$, such that SEDOR on the NV can detect coherent evolution between the NV and spin i. We refer to a dark spin j as a second-layer spin if the coupling strength to a first-layer spin i is $d^{i,j} > 1/T_2^i$ and $d^{\text{NV},j} < 1/T_2^{\text{NV}}$. A chain of spins follows this pattern to successive layers.

2.5 Control sequences

Microwave pulses to control the electronic spin states for the NV or dark spins are incorporated in the Hamiltonian of Equation (2.6) as follows:

$$H(t) = H + 2\Omega_0^{\mathrm{NV}} \cos\left(\omega_{\mathrm{mw}}^{\mathrm{NV}} t\right) S_x + \sum_i 2\Omega_0^i \cos\left(\omega_{\mathrm{mw}}^i t\right) S_x^i. \tag{2.7}$$

We make a transformation into the rotating frame under the following unitary operator:

$$U(t) = \exp\left(-i\omega_{\mathrm{mw}}^{\mathrm{NV}} S_z t - i \sum_i \omega_0^i S_z^i t\right), \tag{2.8}$$

where $H_{rot} = U^\dagger H(t) U - i\partial_t U U^\dagger$. Substituting in $H(t)$ from above, we obtain:

$$H_{rot} = \Delta\omega^{\mathrm{NV}} S_z + \Omega_0^{\mathrm{NV}} S_x + \sum_i \left(\Delta\omega^i S_z^i + \Omega_0^i S_x^i + 2d^{\mathrm{NV},i} S_z S_z^i\right) + \sum_{i,j} d^{i,j} S_z^i S_z^j, \tag{2.9}$$

Where $\Delta\omega = \omega_0 - \omega_{\mathrm{mw}}$ is the detuning from the resonance frequency of the electronic transition. For the following analysis, it will be more convenient to express the spin-1/2 operators in terms of Pauli operators, where now:

$$H_{rot} = \frac{1}{2}\Delta\omega^{\mathrm{NV}} \sigma_z + \frac{1}{2}\Omega_0^{\mathrm{NV}} \sigma_x + \frac{1}{2}\sum_i \left(\Delta\omega^i \sigma_z^i + \Omega_0^i \sigma_x^i + d^{\mathrm{NV},i} \sigma_z \sigma_z^i\right) + \frac{1}{4}\sum_{i,j} d^{i,j} \sigma_z^i \sigma_z^j. \tag{2.10}$$

2.5.1 Spin-echo double resonance (SEDOR)

Here, we show how the spin-echo double resonance sequence using spin i as a probe can be used to characterize a target spin j in its environment. The goal is to measure the resonance frequency of the target spin (ω_0^j), and the dipolar coupling strength between the two spins ($d^{i,j}$) [13]. It is assumed spin i's resonance frequency has already been measured and the spin can be initialized in a pure state. We will see how this can be accomplished for spins outside the first layer by concatenating SEDOR and Hartmann-Hahn Cross Polarization (HHCP) sequences starting with the NV and a first-layer spin. For now, considering only spins i and j which can either be in the same layer or one layer apart, the doubly-rotating frame Hamiltonian during

free evolution is:

$$H_0 = \frac{1}{2}\left(\Delta\omega^i\sigma_z^i + \Delta\omega^j\sigma_z^j + d\sigma_z^i\sigma_z^j\right). \tag{2.11}$$

The control Hamiltonian for either spin during the pulses takes the form (ignoring cross-talk terms):

$$H_{c,(x,y)} = \frac{1}{2}\left(\Omega_0\sigma_{(x,y)} + \Delta\omega\sigma_z\right), \tag{2.12}$$

where we neglect the dipolar coupling term since it is negligible compared to $\Delta\omega$ and Ω_0, and the polarization of the driving term can be switched between the x and y directions by tuning the phase of the pulse in the lab-frame. Initially, the probe spin is polarized along z and the target spin is in a mixed state, which is expressed by the following density matrix (taking I_2 to represent the 2X2 identity operator and I_4 to represent the 4X4 identity operator):

$$\rho_0 = \frac{1}{4}\left(I_4 + \sigma_z^i \otimes I_2\right). \tag{2.13}$$

Evolution of a state ρ under any two-spin Pauli operator A (with $A^2 = I$) for a phase θ is expressed as:

$$\rho \xrightarrow{\theta A} e^{-i\frac{\theta}{2}A}\rho e^{i\frac{\theta}{2}A} = \cos(\theta)\rho - i\sin(\theta)\left[A,\rho\right], \tag{2.14}$$

where we have made use of the the Baker-Hausdoff formula in the last step [45]. If A is a sum of operators, the last step can be applied sequentially so long as these terms commute with each other.

The SEDOR sequence consists of the following steps:

1. $\pi/2$-pulse along y on spin i
2. evolution under the mutual dipolar interaction for a time $T/2$
3. simultaneous π-pulses on spins i and j along x
4. dipolar evolution for a time $T/2$
5. $\pi/2$-pulse along $-y$ on spin i

First, we consider the case where $\Delta\omega^i = \Delta\omega^j = 0$ (on-resonance driving for both spins), and where we sweep the evolution time. We refer to this case as SEDOR-Ramsey(i,j), which allows us to measure the coupling strength between the spins, d. The total evolution of σ_z^i under the SEDOR sequence is then calculated below:

$$\sigma_z^i \xrightarrow{\pi/2\sigma_y^i} \sigma_x^i \tag{2.15}$$

$$\xrightarrow{\frac{dT}{4}\sigma_z^i\sigma_z^j} \cos(dT/2)\sigma_x^i + \sin(dT/2)\sigma_y^i\sigma_z^j \tag{2.16}$$

$$\xrightarrow{\pi\sigma_x^i} \cos(dT/2)\sigma_x^i - \sin(dT/2)\sigma_y^i\sigma_z^j \tag{2.17}$$

$$\xrightarrow{\pi\sigma_x^j} \cos(dT/2)\sigma_x^i + \sin(dT/2)\sigma_y^i\sigma_z^j \tag{2.18}$$

$$\xrightarrow{\frac{dT}{4}\sigma_z^i\sigma_z^j} \cos^2(dT/2)\sigma_x^i + 2\sin(dT/2)\cos(dT/2)\sigma_y^i\sigma_z^j - \sin^2(dT/2)\sigma_x^i. \tag{2.19}$$

And the density matrix becomes:

$$\rho_f = \frac{1}{4}\left(I + \cos^2(dT/2)\sigma_x^i + 2\sin(dT/2)\cos(dT/2)\sigma_y^i\sigma_z^j - \sin^2(dT/2)\sigma_x^i\right). \tag{2.20}$$

The measured signal, $\langle\sigma_z^i\rangle$, is then:

$$\langle\sigma_z^i\rangle = \mathrm{Tr}(\sigma_z^i\rho_f) = \cos^2(dT/2) - \sin^2(dT/2) = \cos(dT). \tag{2.21}$$

Now in order to measure ω_0^j we sweep the detuning $\Delta\omega^j$. We call this experiment SEDOR-ESR(i, j). In this case we are on resonance for the probe spin ($\Delta\omega^i = 0$), and off resonance for the target spin ($\Delta\omega^j \neq 0$) as we sweep the frequency of the recoupling π-pulse. The calculation above is unaffected until the step where the density matrix evolves under $\pi\sigma_x^j$. This will modify the $\sigma_y^i\sigma_z^j$ term in the density matrix as follows:

$$\sigma_y^i\sigma_z^j \to e^{\left(-i\frac{\pi}{\Omega_0^j}H_{c,x}^j\right)}\sigma_y^i\sigma_z^j e^{\left(i\frac{\pi}{\Omega_0^j}H_{c,x}^j\right)} = A\sigma_y^i\sigma_z^j + B\sigma_y^i\sigma_y^j + C\sigma_y^i\sigma_x^j. \tag{2.22}$$

The only term that will contribute to the final signal when taking the trace as above

will be $A\sigma_y^i\sigma_z^j$ (since $\left[\sigma_z^i\sigma_z^j, \sigma_y^i\sigma_z^j\right] = -i\sigma_x^i$). A is computed to be:

$$A = \frac{\left(\Delta\omega^j\right)^2 + \Omega_0^2 \cos\left(\frac{\pi\sqrt{\left(\Delta\omega^j\right)^2+\Omega_0^2}}{\Omega_0}\right)}{\left(\Delta\omega^j\right)^2 + \Omega_0^2}, \tag{2.23}$$

and the final signal is now modified as:

$$\langle\sigma_z^i\rangle = \mathrm{Tr}(\sigma_z^i\rho_f) = \cos^2(dT/2) + A\sin^2(dT/2) = \cos^2(dT/2) + \left(\frac{\left(\Delta\omega^j\right)^2 + \Omega_0^2 \cos\left(\frac{\pi\sqrt{\left(\Delta\omega^j\right)^2+\Omega_0^2}}{\Omega_0}\right)}{\left(\Delta\omega^j\right)^2 + \Omega_0^2}\right)\sin^2(dT/2). \tag{2.24}$$

When $T = \pi/d$, the signal measured produces a sinc line-shape as a function of frequency. The sidepeaks are not detectable at our level of SNR, and thus the resonance signal can be fit to a Lorentzian lineshape to extract ω_0^j.

2.5.2 Hartmann-Hahn Cross Polarization (HHCP)

The Hartmann-Hahn Cross Polarization (HHCP) sequence is used to transfer spin polarization between two spins that are coupled through the dipolar interaction [21]. Since the environmental spins surrounding the NV center are initially at equilibrium (in a mixed state), this provides a mechanism to prepare the dark spins in a pure state through the central optically initialized NV center. As we will see in Chapter 4, this is not limited to the dark spins directly coupled to the NV center. We can concatenate HHCP blocks to transfer polarization across spin chains starting from the NV center to spins in higher layers. To illustrate how the HHCP sequence works, we consider an NV center and a single dark spin that are coupled with coupling strength d. We assume the microwave control is on resonance for both spins, and so the 2-spin Hamiltonian in the doubly-rotating frame is:

$$H = \frac{1}{2}\left(\Omega_0^{\mathrm{NV}}\sigma_x + \Omega_0^i\sigma_x^i + d\sigma_z\sigma_z^i\right). \tag{2.25}$$

We consider the initial state where the NV is polarized and the dark spin is in a mixed state, as represented by the density matrix:

$$\rho_0 = \frac{1}{4}\left(I_4 + \sigma_z \otimes I_2\right), \tag{2.26}$$

The HHCP sequence consists of the following steps:

1. $\pi/2$-pulse along y on the NV

2. simultaneous driving for the NV and spin i along x for a time T

3. $\pi/2$-pulse along $-y$ on the NV

We can skip over the analysis of the $\pi/2$ pulses by considering the transformed Hamiltonian (where $x \to z$ and $z \to -x$),

$$H_t = \frac{1}{2}\left(\Omega_0^{\mathrm{NV}}\sigma_z + \Omega_0^i\sigma_z^i + d\sigma_x\sigma_x^i\right) \tag{2.27}$$

In the computational basis, the Hamiltonian is expressed by the following matrix:

$$H_t = \frac{1}{2}\begin{pmatrix} \Omega_0^{\mathrm{NV}} + \Omega_0^i & 0 & 0 & d \\ 0 & \Omega_0^{\mathrm{NV}} - \Omega_0^i & d & 0 \\ 0 & d & -\Omega_0^{\mathrm{NV}} + \Omega_0^i & 0 \\ d & 0 & 0 & -\Omega_0^{\mathrm{NV}} - \Omega_0^i \end{pmatrix}, \tag{2.28}$$

and we can make the secular approximation since $d \ll \Omega_0$:

$$H_t \approx \frac{1}{2}\begin{pmatrix} \Omega_0^{\mathrm{NV}} + \Omega_0^i & 0 & 0 & 0 \\ 0 & \Omega_0^{\mathrm{NV}} - \Omega_0^i & d & 0 \\ 0 & d & -\Omega_0^{\mathrm{NV}} + \Omega_0^i & 0 \\ 0 & 0 & 0 & -\Omega_0^{\mathrm{NV}} - \Omega_0^i \end{pmatrix}. \tag{2.29}$$

We can block diagonalize the above matrix by reordering the basis states by: $\{|00\rangle, |11\rangle, |01\rangle, |10\rangle\}$:

$$H_t = \frac{1}{2}\begin{pmatrix} \Omega_0^{\mathrm{NV}} + \Omega_0^i & 0 & 0 & 0 \\ 0 & -\Omega_0^{\mathrm{NV}} - \Omega_0^i & 0 & 0 \\ 0 & 0 & \Omega_0^{\mathrm{NV}} - \Omega_0^i & d \\ 0 & 0 & d & -\Omega_0^{\mathrm{NV}} + \Omega_0^i \end{pmatrix}. \tag{2.30}$$

The relevant dynamics then occur in the delta subspace spanned by $\{|01\rangle, |10\rangle\}$, where the two-level system undergoes Rabi oscillations with frequency equal to the dipolar coupling strength and detuning equal to the mismatch in the Rabi frequencies, $\Delta\Omega = \Omega_0^{\mathrm{NV}} - \Omega_0^i$. Although we have assumed both $\Omega_0^{\mathrm{NV}}, \Omega_0^i > 0$, the resulting dynamics will be same but will occur within the $\{|00\rangle, |11\rangle\}$ subspace if we set the driving amplitudes to have opposite polarity (which can be achieved by adding a π-phase difference between the two final $\pi/2$-pulses). For the case where the driving amplitudes have the same sign, the Hamiltonian in the delta subspace is:

$$H_\Delta = \frac{\Delta\Omega}{2}\sigma_z^\Delta + \frac{d}{2}\sigma_x^\Delta \tag{2.31}$$

The signal, $\langle\sigma_z\rangle$, when the initial state is in $|01\rangle$ is the solution to the generalized Rabi problem after evolution for time T:

$$S(T)|_{|01\rangle} = \frac{\Delta\Omega^2 + d^2\cos\left(\sqrt{\Delta\Omega^2 + d^2}T\right)}{\Delta\Omega^2 + d^2}. \tag{2.32}$$

The signal when the initial state is in $|00\rangle$ is $S(T)|_{|00\rangle} = 1$. The total signal is the average of the two:

$$S(T) = \frac{d^2 + 2\Delta\Omega^2 + d^2\cos\left(\sqrt{\Delta\Omega^2 + d^2}T\right)}{2\left(\Delta\Omega^2 + d^2\right)}. \tag{2.33}$$

Since the total spin polarization is constant, we can immediately solve for the polarization of the dark spin:

$$\langle\sigma_z^i\rangle = 1 - S(T) = \frac{d^2 - d^2\cos\left(\sqrt{\Delta\Omega^2 + d^2}T\right)}{2\left(\Delta\Omega^2 + d^2\right)}. \tag{2.34}$$

The polarization transfer is maximized at the matching condition when $\Delta\Omega = 0$, or when $\Omega_0^{\mathrm{NV}} = \Omega_0^i$, where the NV and dark spin signals are:

$$\langle \sigma_z \rangle = \frac{1 + \cos(dT)}{2} \tag{2.35}$$

$$\langle \sigma_z^i \rangle = \frac{1 - \cos(dT)}{2} \tag{2.36}$$

2.5.3 The measurement sequence

For all data presented in this thesis, we perform a differential and normalized measurement of the NV fluorescence. The fluorescence data is collected as an intensity in kilo-counts per second. An arbitrary experimental sequence maps the initial spin-state population of the NV to a final population, which can be expressed in terms of density matrices: $\rho_0 = \frac{1}{2}(I + \sigma_z) \rightarrow \rho_f$. We model the fluorescence readout with a projective measurement operator of the $m_s = 0$ state, expressed as M_0. The four measurement steps of the protocol and corresponding fluorescence values, S_i, are:

1. $\rho_0 \rightarrow \rho_f,\ M_0(\rho_f) : S_+$

2. $\rho_0 \rightarrow \rho_f \xrightarrow{\pi\sigma_x} \rho_f^-,\ M_0(\rho_f^-) : S_-$

3. $M_0(\rho_0) : S_0$

4. $\rho_0 \xrightarrow{\pi\sigma_x} \rho_{-1},\ M_0(\rho_{-1}) : S_{-1}$

Following the material presented in [48], we can show how when combined these four measurements produce the polarization signal, $\langle \sigma_z \rangle = Tr\left((|0\rangle\langle 0| - |1\rangle\langle 1|)\rho_f\right)$. The projective measurement operator for the $m_s = 0$ state is $M_0 = |0\rangle\langle 0|$, and for the for the $m_s = -1$ state is $M_{-1} = |1\rangle\langle 1|$. However, since the NV contrast is not 100% (i.e. population in the $m_s = -1$ state also contributes to the total fluorescence), we generalize the projective operator to be a weighted superposition of the two:

$$M = \alpha M_0 + \beta M_{-1}. \tag{2.37}$$

Substituting the above operator M for M_0 into the four measurement steps we get:

$$S_+ = Tr(\alpha \left|0\right\rangle \left\langle 0\right| \rho_f + \beta \left|1\right\rangle \left\langle 1\right| \rho_f) \tag{2.38}$$

$$S_- = Tr(\alpha \left|1\right\rangle \left\langle 1\right| \rho_f + \beta \left|0\right\rangle \left\langle 0\right| \rho_f) \tag{2.39}$$

$$S_0 = Tr(\alpha \left|0\right\rangle \left\langle 0\right| \rho_0 + \beta \left|1\right\rangle \left\langle 1\right| \rho_0) \tag{2.40}$$

$$S_{-1} = Tr(\alpha \left|1\right\rangle \left\langle 1\right| \rho_0 + \beta \left|0\right\rangle \left\langle 0\right| \rho_0) \tag{2.41}$$

We can then combine the four measurements to obtain $\langle \sigma_z \rangle$ as follows:

$$\frac{S_+ - S_-}{S_0 - S_{-1}} = \frac{Tr\left(\alpha(\left|0\right\rangle \left\langle 0\right| - \left|1\right\rangle \left\langle 1\right|)\rho_f - \beta(\left|0\right\rangle \left\langle 0\right| - \left|1\right\rangle \left\langle 1\right|)\rho_f\right)}{Tr\left(\alpha(\left|0\right\rangle \left\langle 0\right| - \left|1\right\rangle \left\langle 1\right|)\rho_0 - \beta(\left|0\right\rangle \left\langle 0\right| - \left|1\right\rangle \left\langle 1\right|)\rho_0\right)} \tag{2.42}$$

$$= \frac{(\alpha - \beta)Tr(\sigma_z \rho_f)}{(\alpha - \beta)Tr(\sigma_z \rho_0)} = Tr(\sigma_z \rho_f) \tag{2.43}$$

We can carry out the same analysis by also incorporating common mode noise (background fluorescence), which can be modeled by a constant factor times the identity operator. It is easy to see the differential nature of the measurement cancels out this contribution.

Error propagation

We assume the noise associated with the fluorescence signal follows Poisson statistics, where the uncertainty in a single measurement is $\delta S_i \approx \sqrt{S_i}$. Then, following the Central Limit Theorem, as we repeat the measurement N times the uncertainty in the mean, $\overline{S}_i$, is $\delta \overline{S}_i = \sqrt{\overline{S}_i}/N$.

To obtain the total uncertainty for the NV contrast, $\delta\langle \sigma_z \rangle$, where $\langle \sigma_z \rangle = \frac{\overline{S}_+ - \overline{S}_-}{\overline{S}_0 - \overline{S}_{-1}}$, we use the standard error propagation rules [23] to combine the uncertainties associated with the independent averages: $\delta\overline{S}_+$, $\delta\overline{S}_-$, $\delta\overline{S}_0$, $\delta\overline{S}_1$. The uncertainty for the numerator, $\overline{S}_{\text{diff}} = \overline{S}_+ - \overline{S}_-$ and denominator, $\overline{S}_{\text{ref}} = \overline{S}_0 - \overline{S}_{-1}$ are:

$$\delta\overline{S}_{\text{diff}} = \sqrt{\delta\overline{S}_+^2 + \delta\overline{S}_-^2}, \tag{2.44}$$

$$\delta\overline{S}_{\text{ref}} = \sqrt{\delta\overline{S}_0^2 + \delta\overline{S}_{-1}^2}. \tag{2.45}$$

The uncertainty for the polarization signal, $\overline{S}_{\text{diff}}/\overline{S}_{\text{ref}}$, is:

$$\delta\langle\sigma_z\rangle = \langle\sigma_z\rangle\sqrt{\left(\frac{\delta\overline{S}_{\text{diff}}}{\overline{S}_{\text{diff}}}\right)^2 + \left(\frac{\delta\overline{S}_{\text{ref}}}{\overline{S}_{\text{ref}}}\right)^2} \tag{2.46}$$

The error bars for the NV signal data reported in all measurements in this thesis are $\delta\langle\sigma_z\rangle$.

Conversion of NV contrast to dark spin contrast

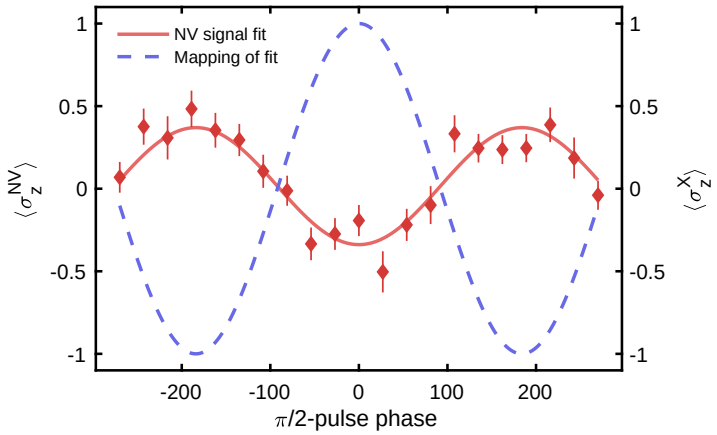

Figure 2-5: NV spin contrast $\langle\sigma_z^{\text{NV}}\rangle$ mapping to the dark spin contrast $\langle\sigma_z^{\text{X}}\rangle$ (where X is the label for a first-layer dark spin to be identified in Chapter 3). Both X hyperfine transitions are driven to address 100% of the electronic spin population for X.

For the SEDOR experiments performed on a dark spin probe which is directly coupled to the NV, we would like to convert the directly measured NV spin polarization to the dark spin polarization by renormalizing to subtract off effects of imperfect control during the HHCP polarization and readout blocks. We can create a mapping from the NV spin contrast, $\langle\sigma_z^{\text{NV}}\rangle$, to the dark spin X_1 contrast, $\langle\sigma_z^{\text{X}}\rangle$, by using the calibration signal displayed in Figure 2-5. This signal measures the full 2π evolution of the dark spin state between the HHCP iSWAP gates (where the spin lock duration T is set to π/d) by sweeping the phase of the second $\pi/2$ pulse on the dark spin during the first HHCP block. The reduction in amplitude of the NV signal after round-trip polarization transfer with the dark spin allows us to assess the fidelity of our microwave control on the dark spin, and will also factor into our estimate for

setting a limit on how many layers of spins we can control in a given network (see Section 4.3).

For this measurement, we fit to the following cosine signal:

$$f(x) = b_0 + A_0 \cdot \cos(2\pi f_0 x), \tag{2.47}$$

where $b_0 = .016(2)$ and $A_0 = -0.35(3)$. We then construct the mapping as:

$$\langle \sigma_z^{\mathrm{X}} \rangle = \frac{\langle \sigma_z^{\mathrm{NV}} \rangle - b_0}{A_0}. \tag{2.48}$$

The uncertainty is calculated as:

$$\delta\langle \sigma_z^{\mathrm{X}} \rangle = \frac{\delta\langle \sigma_z^{\mathrm{NV}} \rangle}{A_0}. \tag{2.49}$$

Chapter 3

Spin network characterization

3.1 System identification with spin-echo double resonance (SEDOR)

Our goal is to map out all terms in the spin Hamiltonian for the network of dark spins surrounding a central NV, within our experimental limits. We generalize the secular spin Hamiltonian in Equation (2.6) to remove the distinction between the NV and dark spins, which can be expressed as:

$$H = \frac{1}{2}\sum_i \omega_0^i \sigma_z^i + \frac{1}{4}\sum_{i\neq j,j} \omega_d^{ij} \sigma_z^i \sigma_z^j. \tag{3.1}$$

As in Equation (2.6), $z = z^{\mathrm{NV}}$ defines the orientation of the external magnetic field aligned with the NV molecular axis. The resonance frequency $\omega_0^i = \gamma_e B_0 + (m_I A)^i$ corresponds to the electron-Zeeman splitting and hyperfine shift in the m_I nuclear spin manifold for the i^{th} spin, and $\omega_d^{ij} = 2\pi d^{ij}$ corresponds to the dipolar coupling strength between the i^{th} and j^{th} spins. Note that now d^{ij} no longer absorbs the factor of 2π as in Chapter 2, and is now expressed in units of Hz.

The general protocol relies on the experimental sequences outlined in Figure 3-1 and Figure 3-4. We first use the NV as a probe to detect and identify potential couplings to first-layer spins via spin-echo double resonance (SEDOR). Once a first-layer spin is identified, this spin can be used as a probe to identify second-layer

spins or its coupling to other first-layer spins. This protocol can be extended to probe for spins in higher layers through recursive application in order to construct the interaction graph for the spin network, i.e. measure all terms in the secular spin Hamiltonian. We will demonstrate in Chapter 4 how spins in higher layers can be used to probe the extended network by transferring spin polarization from the NV outwards along the chain.

The SEDOR sequence requires a mechanism for initialization and readout of the probing spin, which for the NV can be accomplished by applying a laser pulse. However, the environmental dark spins do not feature spin-dependent optical transitions. Thus in order to harness them as probing spins, polarization must be transferred from and to the NV for initialization and readout. This is accomplished with the Hartmann-Hahn Cross Polarization (HHCP) sequence, which consists of simultaneous spin-locking both spins at matched Rabi frequencies [21]. Polarization of a dark spin beyond the first layer can be achieved by concatenating a sequence of HHCP blocks starting with the NV.

While correlation spectroscopy could be used to detect spins in higher layers without polarizing the probing dark spin [45], we ultimately intend to harness these spins in a quantum register, requiring their spin state to be initialized and measured. In order to demonstrate identification and control of a second-layer spin and thus provide a roadmap to extending the system identification to higher layers, we apply our protocol beginning with the NV's coupling to the first-layer spins which we call X_1 and X_2. We then use X_1 as a probe to identify its coupling to an additional spin, which we call Y. With these three dark spins characterized, we can map out the complete graph structure by probing the interactions between X_2 and Y, the NV and Y, and X_2 and X_1. We ultimately find that Y is a second-layer spin and only coupled to X_1, providing us access to a coherent chain consisting of the NV, X_1, and Y.

3.1.1 Detection of first-layer spins X_1 and X_2

Starting with the NV as a probe, we seek to identify the resonance frequencies of the first-layer spins. As we will find that there are multiple first-layer spins, we refer to an

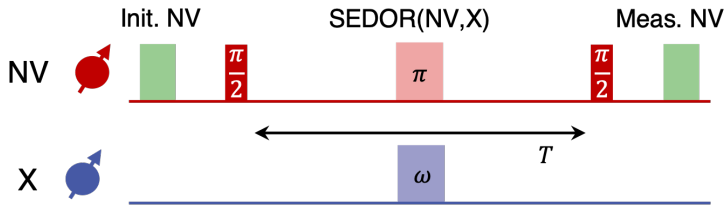

Figure 3-1: The SEDOR(NV,X) experimental sequence is used to identify first-layer spins in the environment of a central NV. The NV is initialized and read out with a green laser pulse, and the m.w. sequence is composed of a spin-echo on the probe spin (NV) with a recoupling π-pulse on the target spin (X). Darker (lighter) shading indicates a pulse along y (x). The recoupling pulse frequency (ω) can be swept for SEDOR-ESR(NV,X) to measure ω_0^{X}, and the recoupling time (T) can be swept for SEDOR-Ramsey(NV,X) to measure $d^{\mathrm{NV,X}}$.

arbitrary first-layer spin as X, and assign an index (e.g. X_1) to a specific spin within the first layer at a given resonance frequency (ω_0^{X1}). The SEDOR control sequence is outlined in Figure 3-1, where a decoupling spin-echo is performed on the NV with a recoupling π-pulse on the potential X target spin. For the SEDOR-ESR experiment, the frequency of the π-pulse is swept around the free electron Larmor frequency, $\gamma_e B_0$, to identify an electron-spin resonance transition at which the signal decreases (thus indicating the existence of a dipolar-coupled first-layer spin). Relying on the analytical SEDOR result from Section 2.5.1, the SEDOR-ESR(i, j) signal with spin i as the probe and spin j as the target takes the following form when $T = 1/(2d^{ij})$:

$$\langle \sigma_z^i \rangle = \frac{(\Delta\omega^j)^2 + (\Omega_0^j)^2 \cos\left(\frac{\pi\sqrt{(\Delta\omega^j)^2+(\Omega_0^j)^2}}{\Omega_0^j}\right)}{(\Delta\omega^j)^2 + (\Omega_0^j)^2}, \tag{3.2}$$

where $\Delta\omega^j = \omega_0^j - \omega_{\mathrm{mw}}^j$ is the corresponding detuning from the target-spin resonance frequency, and Ω_0^j is the target-spin Rabi frequency. When the recoupling time $T \neq 1/(2d^{ij})$, the phase acquired by the probe spin from the dipolar evolution will not be exactly 180°, and so the contrast of the resonance dip will be smaller. Thus when the coupling strength is unknown when first searching for a target spin we perform SEDOR-ESR at several recoupling times before the coherence of the probe spin undergoes significant decay ($\lesssim T_2/2$). The signal $\langle \sigma_z^{\mathrm{NV}} \rangle$ is extracted from the NV fluorescence by performing a differential measurement and normalizing by the

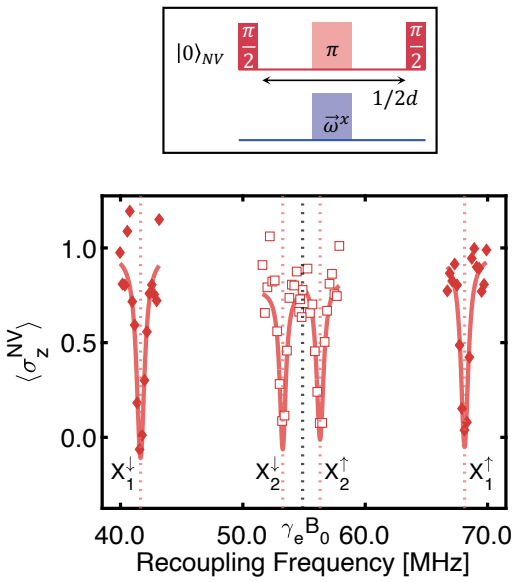

Figure 3-2: The SEDOR-ESR(NV,X) experimental data show the resonance frequencies and hyperfine splittings of the first-layer spins labeled X_1 (A = 26.5(6) MHz) and X_2 (A = 3.0(5) MHz), and confirm both belong to electronic spin-1/2 and nuclear spin-1/2 defects. The x-axis corresponds to the intermediate frequency in our mixer circuit, with an LO frequency of ∼960 MHz. Solid lines are Lorentzian fits to the data (details in Appendix A.1). The pulse sequence above consists of a spin-echo on the probing spin (NV) at fixed evolution time, and a recoupling π-pulse on the target spin (X_1, X_2) at a variable frequency.

NV fluorescence contrast from the $m_s = 0$ and $m_s = -1$ states (see Section 2.5.3 for further details).

Once an X spin is detected in the SEDOR-ESR(NV,X) spectrum, thus identifying ω_0^{X}, we measure the coupling strength, $d^{\mathrm{NV,X}}$, by performing SEDOR-Ramsey(NV,X). This consists of resonantly driving the X spin and sweeping the interaction (recoupling) time. From Section 2.5.1, the analytical signal is $\langle\sigma_z^{\mathrm{NV}}\rangle = \cos\left(2\pi d^{\mathrm{NV,X}} T\right)$, and the coupling strength is extracted by taking the Fast Fourier Transform (FFT) of the signal (see Appendix A.1 for further details). While a resonance dip in the SEDOR-ESR(NV,X) signal at ω_0^{X} can result from multiple degenerate spins, a single dominant peak in the SEDOR-Ramsey FFT verifies the presence of a single spin coupled to the NV at this frequency. Other peaks in the FFT would correspond to degenerate spins at different NV-X coupling strengths.

Figures 3-2 and 3-3 demonstrate this identification protocol for two first-layer

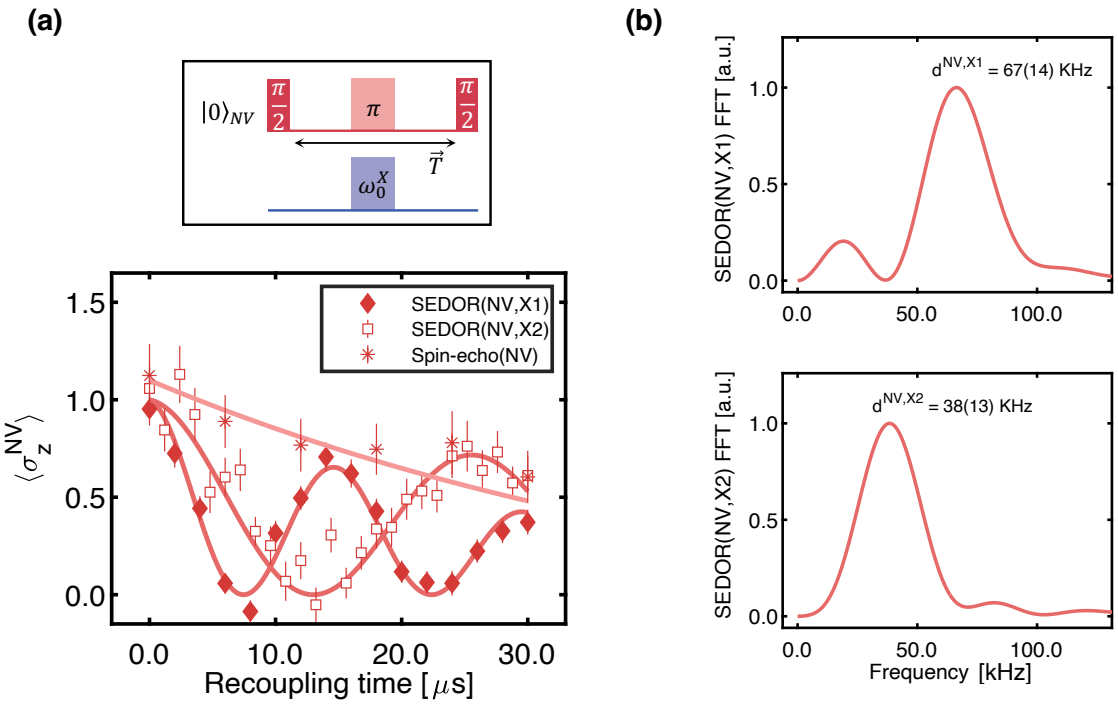

Figure 3-3: (a) The SEDOR-Ramsey(NV,X) experimental data show coherent oscillations mediated by the dipolar coupling between the NV and X spins, and allow us to extract the coupling strengths to the first-layer spins, $d^{\mathrm{NV,X1}}$ and $d^{\mathrm{NV,X2}}$. Here we drive only one hyperfine transition for X, leading to a reduction in contrast by 50%. Also for reference we plot the spin-echo(NV) data, for which we extract the NV coherence time of $T_2^{\mathrm{NV}} = 50(10)\ \mu s$. The pulse sequence above consists of a spin-echo on the probing spin (NV) at swept recoupling time, and a recoupling π-pulse on resonance with the target spin (X_1,X_2). (b) The FFTs of the SEDOR-Ramsey(NV,X) signals reveal single dominant peaks in both spectra and confirm X_1 and X_2 are non-degenerate, with $d^{\mathrm{NV},X1} = 67(14)$ kHz and $d^{\mathrm{NV},X2} = 38(13)$ kHz.

spins. In Figure 3-2 we apply SEDOR-ESR on the NV, and successfully measure the electron-spin transitions corresponding to two spins X_1 and X_2 coupled to the NV, with hyperfine splittings of 26.5(6) MHz and 3.0(5) MHz, respectively. For each spin in the spectrum, there exists two hyperfine peaks of equal intensity, each with half of the total NV contrast. These observations confirm that X_1 and X_2 are electron-nuclear spin defects with S=1/2 and I=1/2 [13, 11].

Next, we perform two different SEDOR-Ramsey experiments on the NV with the recoupling π-pulse on resonance with the $X^{\uparrow}$ hyperfine transition for X_1 and X_2. As we are only addressing half of the electronic spin population, and there is

equal probability to be in either nuclear spin state ($\uparrow$ or $\downarrow$), the expected signal is the average between $\langle\sigma_z^{\mathrm{NV}}\rangle = 1$ and $\langle\sigma_z^{\mathrm{NV}}\rangle = \cos\left(2\pi d^{\mathrm{NV},X}T\right)$. This reduces the contrast by a factor of 2. In Figure 3-3(a) we observe that both the SEDOR-Ramsey signals indeed exhibit this behavior, and oscillate at the coupling strength frequency of 67(14) kHz for X_1 and 38(13) kHz for X_2. Further, the single dominant peak in the accompanying FFT spectra in Figure 3-3(b) conclusively identifies the presence of single spins at the X_1 and X_2 resonances (within the uncertainty of the spectral width).

Additionally, we determine the coherence time of the NV by performing a spin-echo decay measurement, finding a mean-decay time of $T_2^{\mathrm{NV}} \approx 50\ \mu$s (see Appendix A.1 for details of fit). This coherence time sets a lower bound on the coupling strength for a first-layer spin, which is evaluated to be approximately 10 kHz. Having estimated ω_0^{X} and $d^{\mathrm{NV,X}}$ for X_1 and X_2, we have completed the identification steps for both first-layer spins. We now seek to exploit a first-layer spin as a probe to detect and identify a second-layer spin.

3.1.2 Detection of a second-layer spin Y

In an earlier work on this experimental system [48], the presence of coherently interacting spins around X_1 was revealed from characterization of its decoherence, motivating further investigation to realize a larger quantum register. Now, following the above protocol, we identify a second-layer spin Y coupled to X_1.

More concretely, we perform SEDOR as above with X_1 replacing the NV as the probe spin. We refer to this sequence as SEDOR(X,Y). The three-step control sequence is outlined in Figure 3-4. Initialization and measurement of X_1 is accomplished by performing an iSWAP gate between the two spins. An iSWAP gate (a SWAP gate with an additional $\pi/2$ phase) is achieved by setting the HHCP spin-lock duration to $1/(2d^{\mathrm{NV,X1}})$ [10]. For initialization, the laser pulse precedes the HHCP block to prepare the NV in a polarized state. For measurement, the laser pulse follows the HHCP block to read out the NV's polarization. The SEDOR(X,Y) signal, $\langle\sigma_z^{\mathrm{X}}\rangle$, is obtained from the NV fluorescence measurements by converting the NV contrast

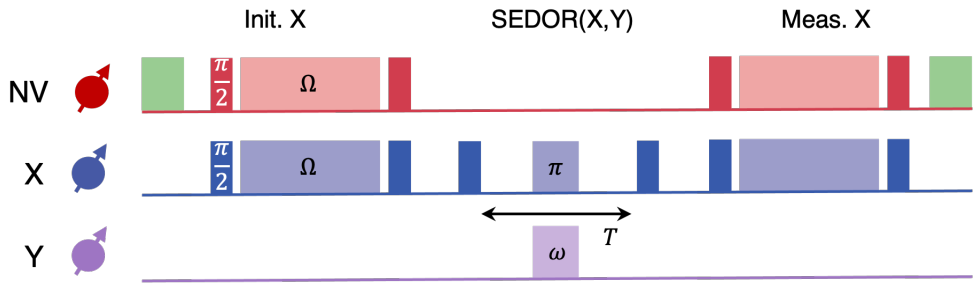

Figure 3-4: The SEDOR(X,Y) experimental sequence is used to identify second-layer spins using X as a probe (where X can be either X_1 or X_2). X is initialized and read out via the NV using HHCP. HHCP consists of simultaneous spin-locking two dipolar-coupled spins at matched Rabi frequencies, and an iSWAP gate can be achieved by setting the spin-lock duration to $1/(2d)$, where d is the dipolar-coupling strength. A second-stage SEDOR sequence is applied between X and Y, where now an initialized X spin is the probe and can be used to characterize a nearby coupled dark spin, Y. The recoupling pulse frequency (ω) can be swept for SEDOR-ESR(X,Y) to measure ω_0^{Y}, and the recoupling time (T) can be swept for SEDOR-Ramsey(X,Y) to measure $d^{\mathrm{X,Y}}$.

according to the calibration mapping presented in Section 2.5.3. We drive both hyperfine transitions of X during the HHCP and SEDOR sequences. This increases the signal contrast in order to compensate for a 50% reduction in signal arising from control imperfections.

The experimental results characterizing the coupling between X_1 and the newly identified Y spin are seen in Figures 3-5 and 3-6. The SEDOR-ESR spectrum of X_1 in Figure 3-5 reveals the resonance frequencies of the two electron-spin transitions of Y, with a hyperfine splitting of 33.5(3) MHz. Following a similar argument from the identification of the X spins above, we conclude that the Y spin belongs to an electronic and nuclear spin-1/2 defect. The SEDOR-Ramsey(X,Y) signal and accompanying FFT in Figure 3-6 characterize the coupling strength, finding $d^{\mathrm{X,Y}} = 20(4)$ kHz, and verify the presence of a single spin at the Y frequency. We choose to truncate our system identification up to a second-layer spin due to setup instabilities that occur over the longer averaging duration required to probe higher layers. However with improved setup stability and control electronics, this protocol can be extended to probe spins in higher layers, and will be discussed in further detail in Chapter 4.

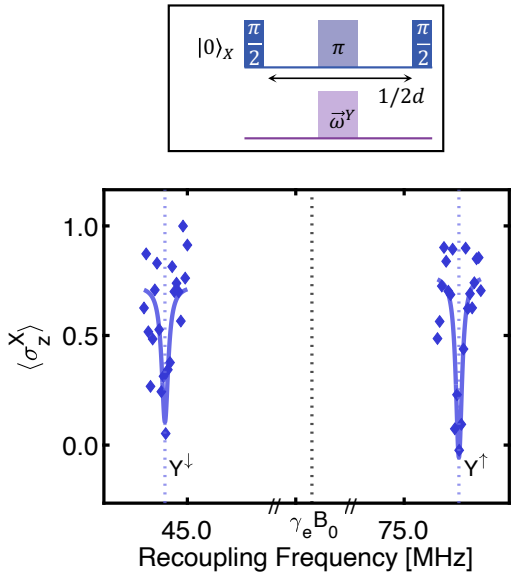

Figure 3-5: The SEDOR-ESR(X_1,Y) experiment uses X_1 as the probing spin to identify the second-layer spin Y. The experimental data show the resonance frequencies and hyperfine splitting of Y (A = 33.5(3) MHz), and confirm it is an electronic spin-1/2 and nuclear spin-1/2 defect. The y-axis scale $\langle\sigma_z^X\rangle$ is normalized and shifted from the NV signal $\langle\sigma_z^{NV}\rangle$ according to the mapping presented in Section 2.5.3.

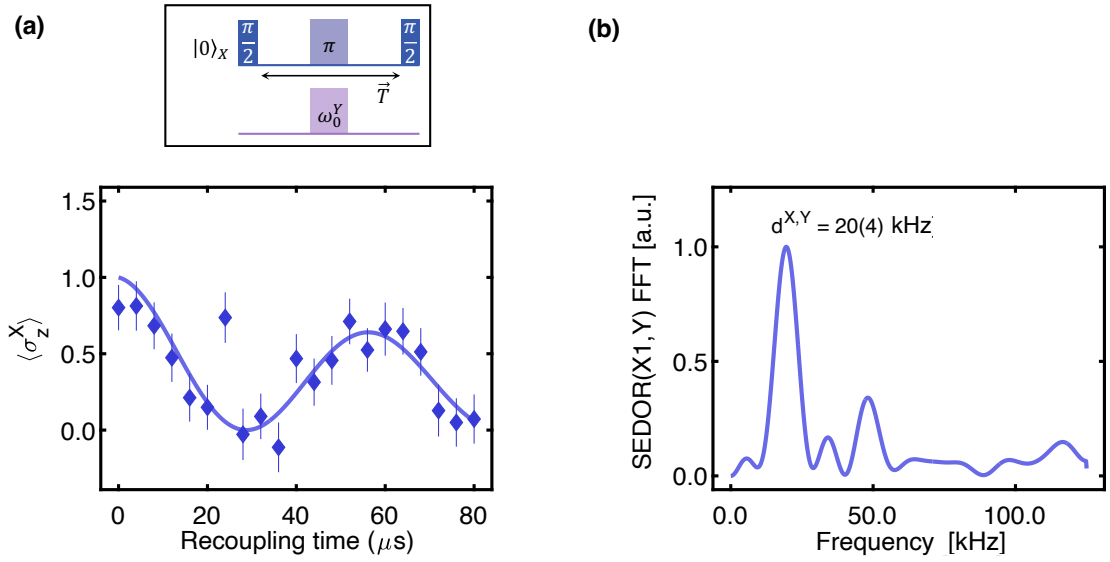

Figure 3-6: (a) The SEDOR-Ramsey(X_1,Y) experiment uses X_1 as the probing spin to measure the coupling strength between X_1 and Y. The experimental data show coherent oscillations mediated by the dipolar interaction. Here we drive only one hyperfine transition for Y, leading to a reduction in contrast by 50%. (b) The FFT of the SEDOR-Ramsey(X_1,Y) data reveals a single dominant peak in the spectrum and confirms Y is non-degenerate, with $d^{X1,Y} = 20(4)$ kHz.

Three distinct types of defects

As explained in Section 2.2, the defect structure depends on the type of impurity atom, the existence and number of nearby vacancies, and relative locations of these impurities and vacancies. These properties are what define the characteristics of the interaction between defect's orbital electronic spins and nuclear spins, which is the hyperfine coupling. The hyperfine tensor expressed in the defect's principal axes in the lattice contain the principal components that are unique for each type of defect.

We remark that the hyperfine components of X_1 and X_2 reported in an earlier work [11] show that they are in fact distinct defect structures and that neither one are consistent with any of the nitrogen or hydrogen defects reported in other works [58, 19, 39]. It should be noted that the current hyperfine splitting of X_2 measured in Figure 3-2 is different than what is reported in [11] at the same external field orientation. However, the current value is still consistent with the previous hyperfine components, so it is possible the defect orientation has changed within the lattice.

Further experiments must be done to fully identify the hyperfine tensor of Y by sweeping the orientation of the external magnetic field. However we claim that from the SEDOR measurement of Y's hyperfine splitting at this particular field orientation, Y must be a different defect type from X_1 and X_2. To support this claim, we solve for the range of hyperfine splitting values for X_1 and X_2 to determine whether either overlaps with the observed splitting of Y. If this were the case, the defect structures could be the same but with different orientations within the lattice.

We first consider how the hyperfine tensor enters into the spin Hamiltonian and thus determines the resonance frequency of the defect's electronic spin transition. The hyperfine contribution in the general spin Hamiltonian is:

$$H_{\text{hyperfine}} = \vec{S}^T \cdot A \cdot \vec{I}, \tag{3.3}$$

where $\vec{S}, \vec{I}$ are the electronic and nuclear spin operators, respectively, and A is the hyperfine tensor. For a uniaxially symmetric hyperfine interaction (which is the case for the NV and both X spins [11]), A can be expressed by its principal components

as:

$$A = \begin{pmatrix} A_\perp & & \\ & A_\perp & \\ & & A_\parallel \end{pmatrix}. \tag{3.4}$$

The hyperfine splitting, A_s, measured in the SEDOR-ESR spectrum can be calculated as [56]:

$$A_s = \sqrt{\vec{n}^T \cdot A \cdot A^T \cdot \vec{n}}, \tag{3.5}$$

where $\vec{n}$ defines the orientation of the external magnetic field relative to the principal direction of the hyperfine matrix. This can be expressed as a function of the external field orientation (or polar angle θ with respect to the principal axes frame), which is [8]:

$$A_s(\theta) = \sqrt{A_\perp^2 \sin(\theta)^2 + A_\parallel^2 \cos(\theta)^2}. \tag{3.6}$$

The hyperfine components for X_1 are: $A_\perp = 17.2(3)$ MHz and $A_\parallel = 29.4(2)$ MHz. The hyperfine components for X_2 are: $A_\perp = 1.6(3)$ MHz and $A_\parallel = 11.2(2)$ MHz [11]. The maximum hyperfine splitting occurs at $\theta = 0$ when the external magnetic field is aligned along the principal hyperfine direction, and corresponds to $A_s^{\max} = A_\parallel$. We assume Y is also axially symmetric, and we measure a hyperfine splitting equal to 33.5(3) MHz, which is greater than the maximum hyperfine splitting of X_1 and X_2. Thus, Y must have a different hyperfine tensor from X_1 and X_2, and we conclude the three dark spins belong to distinct defect structures.

3.1.3 Constructing the graph structure

Up to this point, we have successfully detected three environmental spins around a single NV center: X_1, X_2, and Y. The next step is to figure out how this network of 4 spins is connected, such that we can identify all possible spin-pair couplings, d^{ij} in the Hamiltonian. This is necessary in order to harness the register as a useful quantum device. First, this will help in finding the most efficient route for polarization transfer to distant sensing qubits located in higher layers. The aim here would be to maximize the product of individual coupling strengths for all pairs along a chain out

to the target spin. This will enable faster gate times which would be more robust to control imperfections and decoherence, as well as setup instabilities stemming from a longer total averaging duration. Second, by locating more spin-pair couplings we can increase the total number of spins in the system which can be entangled or harnessed as memory qubits. This would help to increase the sensing performance over systems of equal size but with less connections in the network, given control errors are kept fixed [10].

The results of the SEDOR experiments so far confirm the NV is coupled to X_1 and X_2, and that X_1 is coupled to Y. In order to fully characterize the graph structure we need to check the couplings between the NV and Y, X_2 and Y, and X_2 and X_1. More significantly, by verifying Y and the NV are not coupled (down to the minimum coupling strength threshold), we can confirm Y is indeed a second-layer spin. Checking whether Y and X_2 are coupled would determine whether the four spins are connected in a ring or if there is a chain of three spins with an extra spin (X_2) connected to the NV.

Ruling out coupling between the NV and Y

Our approach to checking whether Y is coupled to the NV is to perform SEDOR-ESR(NV,Y) and to search for a resonant dip (or lack of one) in the NV spectrum near the Y resonance frequency. We perform the measurement with the recoupling time set to the NV's coherence time, T_2^{NV}, which sets the lower bound for the coupling strength of a first-layer spin, $d_{\mathrm{min}} = 1/(2T_2^{\mathrm{NV}}) \sim 10$ kHz. A spin coupled to the NV below this threshold would not be detected by the NV due to the decay in contrast, and would exist outside the coherence limit of the NV. In Figure 3-7, we compare the SEDOR-ESR(NV,Y) signal with the SEDOR-ESR(X,Y) signal to confirm no change in the NV contrast at the Y resonance. Thus we conclude that Y is not coupled to the NV and hence can be characterized as a second-layer spin in the network. The identification of a second-layer spin via X_1 is significant as it enables probing the environment beyond what the NV center can directly access, showing that we are no longer limited by its coherence time.

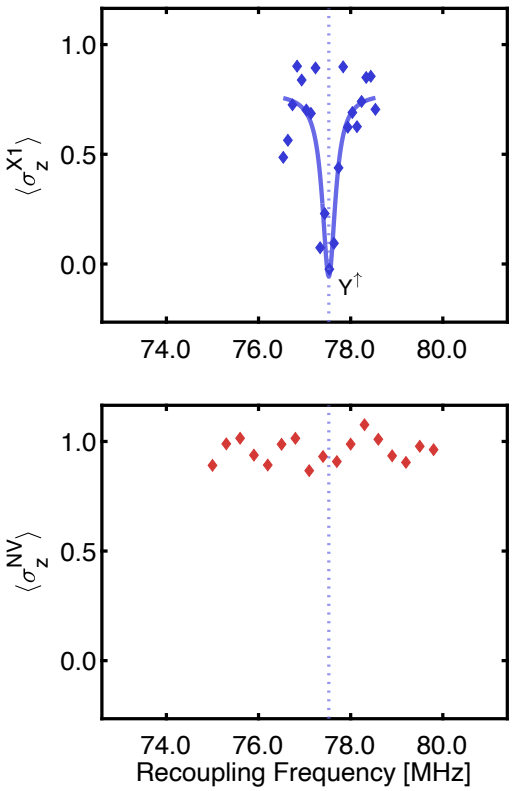

Figure 3-7: SEDOR experiments on the NV and X_1 spins at the Y resonance frequency, showing the NV and Y are not coupled and that Y can be characterized as a second-layer spin. The top plot is adapted from Figure 3-5 and shows the SEDOR-ESR(X_1,Y) resonance signal which locates ω_0^{Y}. The bottom plot shows the results of the SEDOR-ESR measurement on the NV performed at a recoupling time of T_2^{NV} (threshold for coupling to a first-layer spin), with no resonance signal at the Y frequency. The data is shifted to account for the decoherence of the NV during the spin-echo decay.

Ruling out coupling between X_2 and Y

Next we probe for any potential coupling between X_2 and Y. The existence of this additional coupling would create an opportunity for more complex demonstrations using the electronic spin register. One such demonstration would be to perform round-trip polarization transfer over a ring of spins to explore the use of environmental spins as communication links for distant qubits. This can effectively be simulated on a chain of spins by reversing the direction of polarization transfer at the ends, but it is more desirable to increase the number of unique spins in the chain.

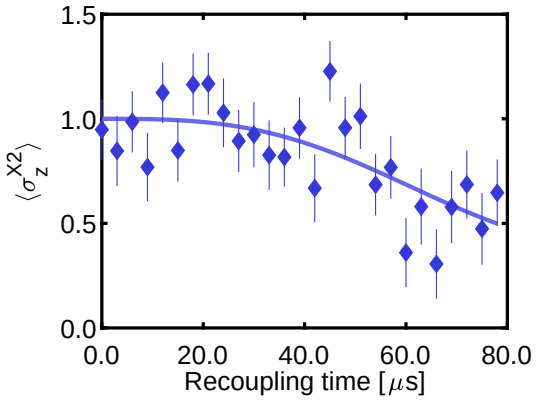

Figure 3-8: SEDOR experiment with X_2 as the probing spin to rule out its coupling to Y. The SEDOR-Ramsey(X_2,Y) experiment shown applies the recoupling pulse on resonance with the Y frequency as the interaction time is swept. The data together with the fitted exponential decay (details in Appendix A.1) rule out coherent oscillation with a single spin at the Y frequency. The outliers to the fit may be the result of X_2 control imperfections or several degenerate Y spins coupled to X_2 with different coupling strengths. We apply the same scaling for $\langle\sigma_z^{X2}\rangle$ to convert from $\langle\sigma_z^{NV}\rangle$ as we do for the X_1 signal.

We perform SEDOR using X_2 as the probing spin with the recoupling-pulse frequency on resonance with Y, and search for evidence of coherent evolution of X_2. Since the coherence time of X_2 was not directly measured and thus the coupling strength threshold for a spin within its coherence limit is unknown, we choose to perform a SEDOR-Ramsey measurement. For this, the recoupling pulse is on resonance with a single Y transition and the recoupling time is swept until the X_2 contrast decays. The result of this experiment is shown in Figure 3-8. The signal appears to decay monotonically according to the fit, which suggests Y is not coupled to X_2. While there appears to be a significant amount of outliers relative to the fitted curve, there does not appear to be a single dominant frequency in the signal. One potential reason for these outliers is the instability of X_2 control, as we find that increasing the number of measurements does not help with the convergence of the signal. Another possibility is that these fluctuations may be a physical phenomenon, suggesting X_2 is coupled to several degenerate spins at the Y resonance frequency (where different frequencies in the signal would be associated with different X_2-Y coupling strengths). A greater number of degenerate spins would contribute to a smaller total contrast

in the signal, making it hard to distinguish coherent evolution from noise. However, since the SEDOR-Ramsey(X_1,Y) data in Figure 3-6 does not feature a similar behavior, we can conclude X_1 and X_2 are located in different regions relative to the NV and experience interactions from different environmental spins. Thus any of the possible Y spins detected through X_2 would not include the single Y spin that is detected through X_1. We use this line of reasoning to claim X_2 and Y (as identified through X_1) are not coupled, but further characterization of the X_2 environment would help to further verify this.

Ruling out coupling between X_1 and X_2

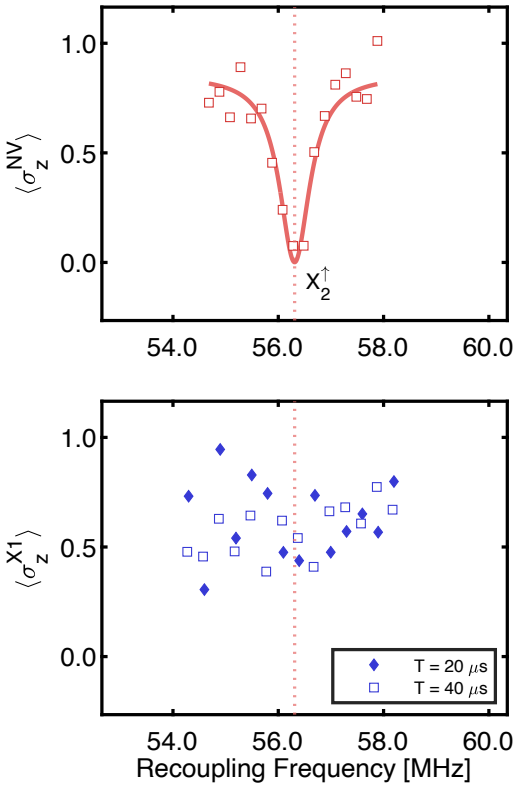

Figure 3-9: SEDOR-ESR experiment with X_1 as the probing spin to rule out its coupling to X_2. The SEDOR-ESR(X_2,X_1) experiment is performed at $T = 20$ μs and $T = 40$ μs and compared with the X_2 resonance signal as detected through the NV (adapted from Figure 3-2 and displayed above). The lack of contrast in the X_1 signal at the X_2 frequency confirms the two first-layer spins are not coupled.

The last step is to check the potential coupling between X_1 and X_2. For this

we perform SEDOR-ESR(X_1,X_2) and probe for any change in X_1 contrast at the X_2 resonance. The experimental data is shown in Figure 3-9, where we directly compare the result with the SEDOR-ESR(NV,X_2) resonance signal. We check the SEDOR-ESR(X_2,X_1) experiment at two different recoupling times, $T = 20$ μs and $T = 40$ μs. The $T = 40$ μs experiment probes for X_2 coupling close to coherence-limit threshold for X_1, assuming a similar coherence time as the NV. The $T = 20$ μs data checks that $d^{X1,X2}T \neq 1$ when $T = 40$ μs. The lack of any resonance signal at ω_0^{X2} for both experiments confirms the two first-layer spins are not coupled.

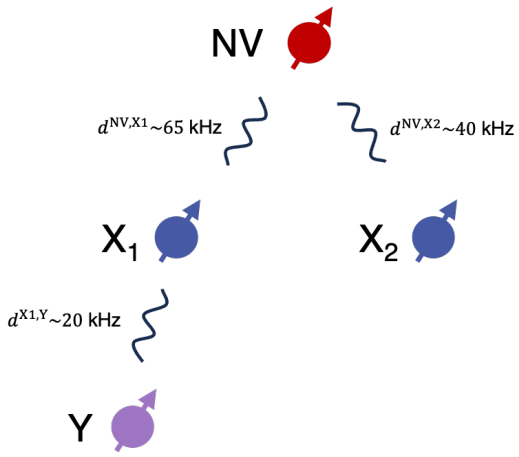

Figure 3-10: Illustration of the spin-graph structure as characterized using SEDOR for the system of four spins consisting of the central NV, and environmental dark spins X_1, X_2, and Y. To summarize, X_1 and X_2 are first-layer spins directly coupled to the NV and not coupled to each other. Y is a second-layer spin directly coupled to X_1 and not coupled to the NV. The NV, X_1, and Y spins form a chain since Y and X_2 are not coupled.

The system identification protocol for the four-spin network using SEDOR is complete now that we have measured the resonance frequency for each spin and the coupling strengths for all possible spin-pair couplings. The resulting graph structure for the network takes the form depicted in Figure 3-10. The chain of three spins (NV, X_1, and Y) will be the focus of our work in the next chapter. There, we rely on the characterization of the second-layer spin to extend control of our electronic spin register beyond the coherence limit of the central NV.

3.2 Nuclear spin identification with ENDOR

Considering the earlier work in constructing the hyperfine tensors for X_1 and X_2 [11], there does not appear to be any reported defects that feature consistent hyperfine components for either. In order to find a potential match, we must consider all possible paramagnetic point defects in diamond which have a uniaxially symmetric hyperfine tensor, and are electronic spin-1/2 and nuclear spin-1/2. While the various nitrogen-related defects have been more closely considered (since the sample was implanted with nitrogen), it may be possible that the impurity atom is hydrogen or silicon which also have nuclear spin-1/2 isotopes [25]. The hydrogen-related War2 defect is shown to have experimentally measured hyperfine components that are similar to X_1 [8]. Both the nitrogen-related War10 defect and hydrogen-related H1 defect have numerically predicted and experimentally measured hyperfine values which are similar to X_2 [2, 58]. Further, the discrepancy between the numerical and experimental hyperfine values for War10 suggests there is a larger uncertainty window in which the X_2 values could also be consistent. We would first like to narrow down the search space for potential defect matches by identifying the nuclear spin species for X_1 or X_2. It may also be possible that we are able to rule out a match with any previously reported defects and claim that X_1 or X_2 is truly a novel defect. Also, identifying the nuclear spin species would enable resonant control of the nuclear spin state and further expand the number of qubits in the register. And with both electronic spin and nuclear spin control we can make use of their complementary advantages, e.g. better sensitivity with the electronic spins and longer coherence with the nuclear spins.

To identify the nuclear spin of either defect, we rely on a measurement sequence based on electron-nuclear double resonance (ENDOR) [45]. This sequence converts coherent evolution of the nuclear spin to a change in electronic spin polarization. The spin Hamiltonian for the two spin system with uniaxial hyperfine coupling is:

$$H = \gamma_e B_0 S_z - \gamma_n B_0 I_z + A S_z I_z + B S_z I_x \tag{3.7}$$

For an S = 1/2 and I = 1/2 defect, the electronic spin transition frequencies are[1]:

$$\omega_e^0(|00\rangle \rightarrow |10\rangle) = \gamma_e B_0 + \frac{1}{2}\sqrt{A^2 + B^2} \tag{3.8}$$

$$\omega_e^1(|01\rangle \rightarrow |11\rangle) = \gamma_e B_0 - \frac{1}{2}\sqrt{A^2 + B^2}, \tag{3.9}$$

and the nuclear spin transition frequencies are:

$$\omega_n^1(|10\rangle \rightarrow |11\rangle) = \sqrt{\left(\frac{A}{2} - \gamma_n B_0\right)^2 + \left(\frac{B}{2}\right)^2} \tag{3.10}$$

$$\omega_n^0(|00\rangle \rightarrow |01\rangle) = \sqrt{\left(\frac{A}{2} + \gamma_n B_0\right)^2 + \left(\frac{B}{2}\right)^2}. \tag{3.11}$$

The general ENDOR experiment can be implemented as follows:

1. initialize electronic spin in $|0\rangle$ with the total system in $|00\rangle$ or $|01\rangle$
2. apply a selective m.w. π-pulse for the $|00\rangle \rightarrow |10\rangle$ transition at frequency ω_e^0
3. apply an r.f. pulse at swept frequency
4. apply a selective m.w. π-pulse for the $|00\rangle \rightarrow |10\rangle$ transition at frequency ω_e^0
5. measure electronic spin population in $|0\rangle$

When the r.f. pulse is on resonance with ω_n^0 or ω_n^1, the contrast in electronic-spin population will be 50% the maximum value if the pulse length corresponds to a perfect π-pulse. Since the nuclear spin transition frequency depends on the nuclear spin gyromagnetic ratio, γ_n, we are able to uniquely determine the defect's nuclear spin species from this measurement.

To initialize and measure the electronic spin state of the defect, we use the HHCP protocol to transfer polarization with the NV electronic spin. We apply simultaneous driving of both hyperfine transition frequencies to address both nuclear spin states. Our sequence then consists of: HHCP(NV,X) $\rightarrow$ selective m.w. π-pulse $\rightarrow$ r.f. pulse $\rightarrow$ HHCP(X,NV). Instead of directly applying the m.w. π-pulse on one of the electronic transitions for X, we add an extra 180° phase between the second $\pi/2$-pulses

[1] assuming $|\gamma_n B_0| \ll A, B$

for the X frequencies during the 1st HHCP block. We calibrate the r.f. power by performing a Rabi measurement on the nitrogen nuclear spin of the NV center (Figure 3-12), which is polarized by laser illumination at our current field strength [38]. To probe for different nuclear spin species, we scale the π-pulse length by the relative gyromagnetic ratio to nitrogen.

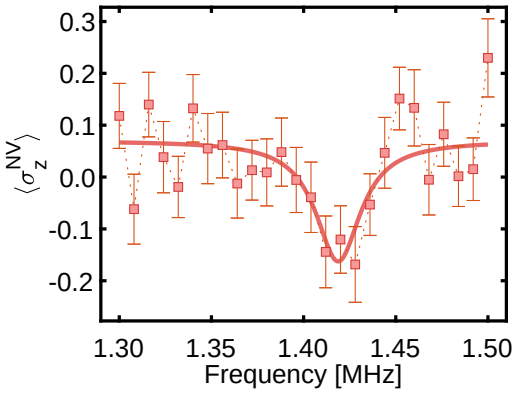

Figure 3-11: ENDOR experiment on the X_2 defect with a 32 μs π-pulse calibrated for the nitrogen nuclear spin. The resonance frequency extracted from the fit at 1.42(2) MHz confirms the X_2 nuclear spin is nitrogen.

The results for the ENDOR measurements on X_2 are shown in Figures 3-11 and 3-12. We first probe for the presence of nitrogen by sweeping the frequency around the nuclear transition frequency in Equation (3.10) corresponding to the nitrogen gyromagnetic ratio, and using the calibrated π-pulse length for the NV nitrogen spin. Since we cannot measure A and B separately we can bound the potential resonance frequency window by Taylor expanding ω_n^1 for $|\gamma_n B_0| \ll A, B$:

$$\omega_n^1 \approx \frac{\sqrt{A^2+B^2}}{2} - \frac{A}{\sqrt{A^2+B^2}}\gamma_n B_0. \tag{3.12}$$

From the SEDOR(NV,X_2)-ESR measurements in Figure 3-2, the hyperfine splitting is $(1/(2\pi))\sqrt{A^2+B^2} = 3$ MHz. And for the nitrogen-15 nuclear spin, $(\gamma_n/(2\pi))B_0 = 0.16$ MHz. Since $0 \leq \frac{A}{\sqrt{A^2+B^2}} \leq 1$, $\omega_n^1/(2\pi)$ should approximately be between 1.3 MHz and 1.5 MHz. The ENDOR measurement vs. frequency signal in Figure 3-11 shows a resonance dip in the NV contrast at 1.42(2) MHz, confirming that the X_2 defect consists of a single nitrogen nuclear spin.

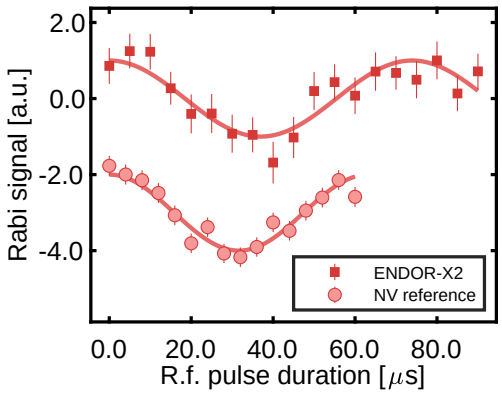

Figure 3-12: Comparing the NV-nuclear spin Rabi measurement with the ENDOR-Rabi measurement on X_2. For ENDOR, the r.f. pulse is applied on resonance with the X_2 nitrogen nuclear spin transition. The Rabi frequencies extracted from the cosine fits are 15.8(5) kHz and 13.5(4) kHz for the NV and X_2 nuclear spins, respectively, further confirming X_2 is comprised of a nitrogen nuclear spin.

We can further verify the presence of nitrogen for the X_2 defect by using ENDOR to perform a nuclear Rabi measurement and comparing the result with the NV's nuclear Rabi measurement. Driving at the nuclear resonance frequency extracted from Figure 3-11, we sweep the r.f. pulse length in the ENDOR sequence and observe Rabi oscillations at a comparable frequency to the NV-nuclear Rabi signal. For the X_2 defect to have a nuclear spin other than nitrogen, the Rabi frequency would need to be at least two times greater than the NV-nuclear Rabi frequency. This corresponds to the spin-1/2 isotope of Si-29 with twice the gyromagnetic ratio compared to N-15.

Together, these results confirm the long held assumption that the X_2 defect is nitrogen-related which formed as a result of the implantation process. Additionally, performing ENDOR measurements at different field orientations may yield new estimates on the hyperfine components which can then be compared with the WAR10 defect. It may be possible the previous hyperfine tensor measurements for X_2 using SEDOR included some systematic uncertainty that is not present with the ENDOR technique. We are currently unable to perform ENDOR on the X_1 defect due to an unexpected instability in the NV fluorescence when applying the r.f. pulse near the nuclear spin transition frequency. However, detection of the nitrogen spin for X_2 further supports the assumption that X_1 is also nitrogen-related.

Chapter 4

Achieving universal control of a second-layer spin

Our results from Chapter 3 show that we can detect and characterize an environmental spin indirectly coupled to a central NV. This relied on the successful application of our novel protocol to perform double resonance measurements between two dark spins, which can be extended to any number of spins in a network without being limited by the coherence time of the central spin. Our goal is to implement the steps required for universal control on spins in this larger coherence volume such that they may be harnessed as qubits in the register. The criteria necessary to achieve universal control for a qubit are initialization, unitary control, and readout [16]. We aim to demonstrate these three steps using the second-layer spin Y, but the approach works the same for spins in higher layers so long as they can be connected back to the NV. For these measurements we will focus on the spin-chain connecting the NV, X_1, and Y spins and use Hartmann-Hahn Cross Polarization to polarize Y. Once Y is polarized, we achieve unitary control through a resonant microwave pulse of variable length to detect Rabi oscillations. Since X_2 will no longer be included in these measurements, we will refer to the X_1 spin as X going forward.

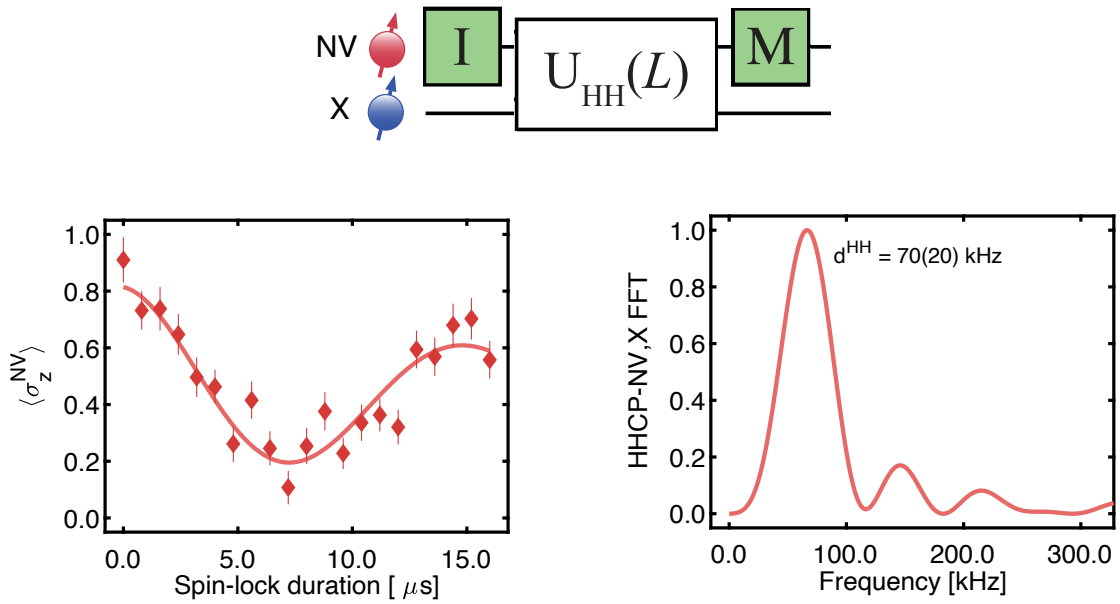

Figure 4-1: Quantum circuit and experimental data demonstrating polarization transfer between the NV and X spins via HHCP. The polarization of the NV, as measured by $\langle \sigma_z^{\mathrm{NV}} \rangle$, reaches a minimum near the iSWAP time of $1/(2d^{\mathrm{NV,X}})$, leaving X in a polarized state. The FFT spectrum characterizes the frequency of polarization transfer, which is consistent with the dipolar coupling strength as measured in SEDOR (Figure 3-3). The I and M blocks in the quantum circuit represent laser pulses to initialize and measure the NV.

4.1 Initialization of the spin chain

Our approach to initialize Y is through sequential polarization transfer across the spin-chain. This consists of two HHCP blocks, the first between the NV and X spins to initialize X (HHCP(NV,X)), and the second between the X and Y spins to initialize Y (HHCP(X,Y)). We begin by characterizing the polarization transfer via HHCP between the NV and X spins by sweeping the simultaneous spin-locking duration. The experimental results are shown in Figure 4-1. The NV signal oscillates at the expected frequency of the dipolar coupling strength measured between the two spins [10]. Since the X spin is initially in a mixed state, the maximum total contrast is half of the full NV contrast, as explained in Section 2.5.2. The signal does not reach zero due to control imperfections, which is strongly dependent on mismatches in the Rabi frequencies and the detuning of the microwave frequency. The signal minimum

corresponds to the time at which we achieve an effective iSWAP gate to initialize X.

We then characterize the HHCP sequence between X and Y by repeating the above protocol, but with X initialized and read out using HHCP(NV,X). In between the HHCP(NV,X) blocks we apply a variable-duration HHCP(X,Y) block. The signal $\langle\sigma_z^{\mathrm{X}}\rangle$ shown in Figure 4-2 also oscillates at the expected dipolar coupling strength frequency, $d^{\mathrm{X,Y}}$. This oscillation indicates polarization is being transferred from X to an environmental spin (or spins). We confirm this experiment achieves coherent spin exchange between X and Y, and thus Y becomes polarized, by observing that the fitted signal contrast of 0.7(1) is consistent with the SEDOR-ESR(X,Y) contrast of 0.760(6) in Figure 3-5 (where both signals are normalized by the same method presented in Section 2.5.3). Thus, at the signal minimum, Y is maximally polarized to within our control limitations, and we have achieved sequential polarization transfer across the spin-chain. Using this result, we can construct an iSWAP gate between X and Y to implement the initialization and readout steps necessary to demonstrate universal control of this second-layer spin.

4.2 Unitary control and detection of Y

We satisfy the requirements of unitary control and readout of Y by further experimentally verifying the polarization of Y after sequential HHCP blocks and measurement of X. This can be understood by first observing in Figure 4-2 that we recover the initial state of X after applying a HHCP block between X and Y with spin-lock duration equal to $1/d^{\mathrm{X,Y}}$, hence performing a round-trip polarization transfer across the chain. This sequence is equivalent to implementing two consecutive iSWAP gates between X and Y. By selectively driving Y with a resonant m.w. pulse at ω_0^{Y} in between the two iSWAP gates, the measured state of X after the second iSWAP will be different from the initialized state of X. Therefore any change in the signal after mapping the state of X back to the NV via HHCP(X, NV) will correspond to a single-qubit rotation of Y.

The experimental result is shown in Figure 4-3. We sweep the m.w. pulse length

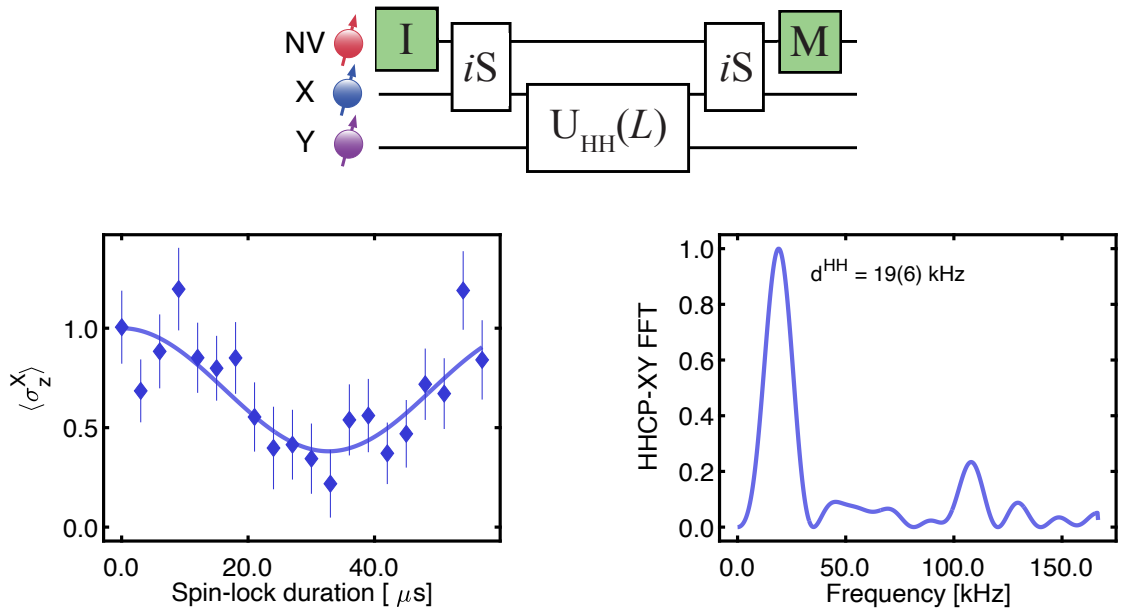

Figure 4-2: Quantum circuit and experimental data demonstrating polarization transfer between the X and Y dark spins via HHCP. The polarization of X, as measured by $\langle\sigma_z^{\mathrm{X}}\rangle$, reaches a minimum near the iSWAP time of $1/(2d^{\mathrm{X,Y}})$, leaving Y in a polarized state, and confirms the successful implementation of cascaded polarization transfer to initialize Y. The signal is normalized as for SEDOR-X, and an additional offset is added such that the maximum fit value equals 1 (see Appendix A.1 for further details). The FFT spectrum shows the frequency of polarization exchange is at the expected dipolar coupling strength, $d^{\mathrm{X,Y}}$. The iS blocks in the quantum circuit represent iSWAP gates between 2 spins implemented using HHCP set to a spin-lock duration of $1/(2d)$.

to perform a Rabi experiment on Y and observe two full oscillations in the NV signal corresponding to a 4π rotation on Y with negligible decay. This signal contrast is further evidence that Y is indeed polarized by applying two sequential HHCP blocks (NV to X, and X to Y), and the resonant m.w. driving on Y achieves single-qubit control. Finally, the observed NV signal can be used to identify the different spin states of Y, thus highlighting that we achieve a mechanism for readout through the NV fluorescence. For example, at $T = 1$ μs the Y spin is inverted 180 °, which corresponds to applying a π-pulse at the given driving strength. At $T = 0.5$ μs the Y spin is in an equal superposition between polarization states, which corresponds to applying a $\pi/2$-pulse. With all three criteria satisfied for universal control of the second-layer spin Y, we enable solid-state registers to include previously inaccessible spins in the

environment of the NV center. And by implementing single-qubit quantum sensing protocols with a second-layer spin, we can increase the detection volume for single spin magnetometry [49, 43].

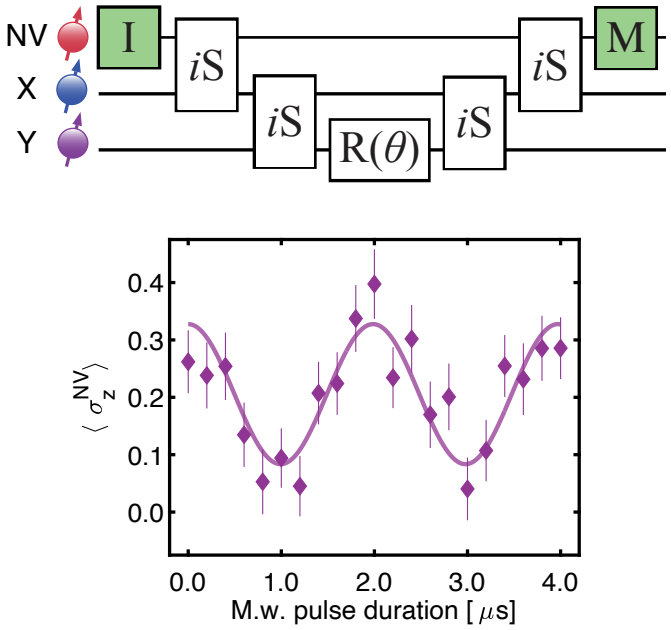

Figure 4-3: Achieving unitary control of Y by detecting Rabi oscillations. Y is initialized and read out by applying sequential iSWAP gates along the chain, using the HHCP(NV,X) and HHCP(X,Y) gates calibrated from the signals in Figures 4-1 and 4-2. We apply a microwave (m.w.) pulse of swept duration on resonance with the Y electronic spin transition to drive Rabi-oscillations. The y-axis scale is the NV contrast, and creates a mapping of the Y spin state for readout. The R(θ) block in the quantum circuit represents a pulse of length $L = \theta/\Omega_0^{\mathrm{Y}}$ where $\Omega_0^{\mathrm{Y}} = 0.5$ MHz.

Finally, we characterize the optical stability of Y, as done similarly for X in a previous work [10]. We do so by measuring the depolarization time of Y during laser illumination. Figure 4-4 shows the polarization of Y decays with a mean lifetime of $T_1^{\mathrm{laser}} = 120(20)$ μs, enabling repetitive readout over this timescale. We can therefore harness this spin as a quantum memory and achieve simultaneous polarization of multiple environmental spins to realize more powerful sensing protocols with the NV center [28, 38].

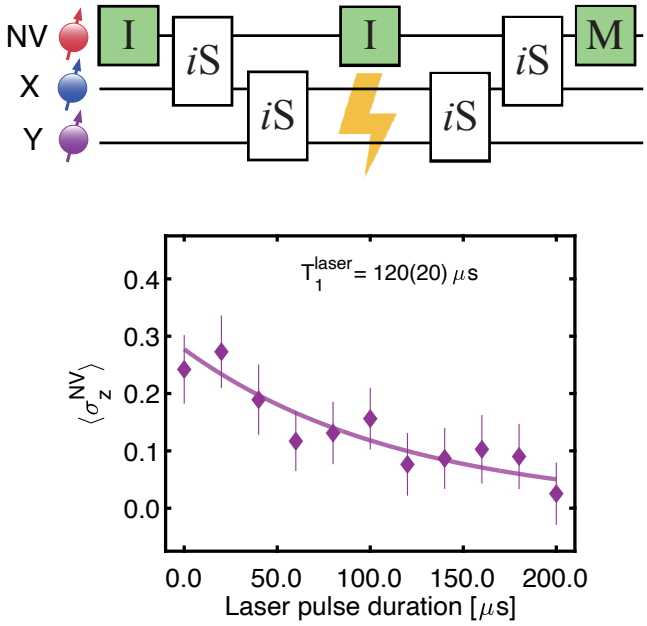

Figure 4-4: Measuring the T_1 decay time of Y under laser illumination, which shows stability over a long enough time scale (a few times the typical iSWAP gate length) to enable repetitive readout and an additional memory qubit in the register.

4.3 Scaling the register to larger networks of spins

Here we investigate what the practical limit is to scaling our register to spins in higher layers. While we have restricted our spin system to include a chain up to the second layer, our results pave a clear path to extending the network to spins in higher layers as well as to multiple spins per layer. We can apply SEDOR to probe for distinguishable spins in the N^{th} layer by concatenating (N-1) HHCP blocks starting with the NV up to the probing spin in the $(N^{\text{th}} - 1)$ layer. In this way, the number of control blocks scale linearly with the number of layers. Our protocol can hence be applied recursively such that the experimental resources required (defined by the number of simultaneous spin transitions driven) remain fixed. Additionally, we can identify new distinguishable spins in a given layer using the same SEDOR sequence over a different resonance frequency range.

We would like to find what the maximum layer number is in which a spin can be detected and controlled using our approach. We refer to this as the network depth.

By achieving control of a dark spin beyond the coherence limit of the NV, we show the size of the network is not limited by the coherence time of our central spin. Further, since the NV can be repolarized, the total experimental time (and hence the number of layers which can be controlled) is not limited by its T_1 relaxation. As the protocol can be constructed recursively to control spins beyond the second-layer through polarization transfer, the T_1 relaxation and T_2 coherence times of any of the dark spins in previous layers will also not limit the depth. Therefore, we are only limited by the decoherence of and controls errors on a spin that is undergoing microwave driving.

We consider such effects by estimating the coherence remaining on the central spin after round-trip polarization transfer along a chain up to a spin in the the N^{th} layer. This consists of N sequential HHCP blocks for initialization and another N for readout. The single HHCP block gate time for a pair of spins between the j^{th} and $(j^{\text{th}}-1)$ layers is $T^j_{\text{SWAP}} = 1/(2d^j)$ and the decoherence time under spin-locking is $T^j_{1,\rho}$. The remaining NV signal after $2N$ SWAPs is:

$$\langle \sigma_z^{\text{NV}} \rangle = e^{-\sum_j^{2N} T^j_{\text{SWAP}}/T^j_{1,\rho}} \tag{4.1}$$

We can substitute typical values for T^j_{SWAP} and $T^j_{1,\rho}$ to consider the scaling with respect to N. We use approximate values extracted from the experimental signal for HHCP(NV,X) in Figure 4-1, with $T^j_{\text{SWAP}} \approx 10$ μs and $T^j_{1,\rho} \approx 100$ μs. Thus,

$$\langle \sigma_z^{\text{NV}} \rangle = e^{-\sum_j^{2N} 0.1} = e^{-0.2N} \tag{4.2}$$

Setting the threshold for a minimum detectable signal to 10% of the maximum NV contrast, we find we can scale up to N $\approx$ 11 layers. However, control imperfections will further reduce this estimate. By including an efficiency η for each SWAP gate, the final signal is then:

$$\langle \sigma_z^{\text{NV}} \rangle = e^{-0.2N} \eta^{2N} \tag{4.3}$$

The SWAP efficiency between the NV and X spins is estimated from the calibration

measurement in Figure 2-5, where we observe a reduction in NV signal by a factor of 2 over 2 SWAP gates, setting $\eta^2 = 0.5$. This reduces the network depth to $N \approx 2$ layers. This shows control imperfections have a significant effect on limiting the size of the spin-register.

Chapter 5

Conclusion and Outlook

In this thesis we have developed and experimentally demonstrated system identification and control protocols to extend the electronic-spin register beyond the coherence limit of the central NV. Additionally, we apply these protocols to map out the graph structure of a four-spin network, and show how this can be extended in a practical manner to larger networks. By identifying larger spin networks of environmental spins, our approach to implementing universal control for a spin beyond the NV coherence limit can be applied recursively to higher layers to achieve more powerful quantum registers. A several-layer electronic spin-chain may enable novel applications in quantum sensing, such as single molecule imaging and correlated spatio-temporal sensing [42, 57, 54, 50, 44, 49], as well as efficient quantum communication via spin-chain wires [35, 33].

Our method is significant as building a larger network of electronic spins is critical to realizing more powerful quantum applications. In quantum sensing, larger spin networks would help increase the metrological gain achieved using entangled states of electronic spins [10]. In quantum communication, larger dark spin chains that are stable under optical illumination would enable efficient transfer of information for larger distributed networks and distant registers [35, 3, 33]. Furthermore, the presented approach is complementary to existing approaches to characterizing and constructing nuclear spin registers [7]. These two approaches can be combined to take advantage of their complementary strengths to enable more powerful hybrid

registers, where each electronic spin in the network can access its own network of nuclear spins [51].

Lastly, we remark that our approach to scale an electronic-spin register relies on exploiting distinct electron paramagnetic species which can be individually controlled. A promising result of our current and previous work in studying the environment of this particular NV center is that we have discovered potentially three unique spin defects formed in the diamond lattice. And since all three defects feature only electronic and spin degrees of freedom, the different electron-nuclear spin couplings allow for stable and distinguishable m.w. control. By combining extensive computational studies [39] with our protocol to identify and control more distinct defects in diamond, we offer a more scalable approach over harnessing identical defects such as P1 centers [15]. To individually initialize and control identical P1s, they must be prepared in different molecular and Jahn-Teller orientations, limiting the total number of individual spin transitions. In this way, we believe our work will be a significant step towards realizing a practical and more capable hybrid electron-nuclear spin register for quantum information processing.

In future work, we aim to make use of our fabricated array of single NVs to explore the advantages of parallel control and detection of individually distinguishable quantum sensing probes. We will integrate a detector array of single-photon avalanche diodes (SPAD array [55]) into the detection path to achieve simultaneous single NV imaging with micron resolution. This will enable us to probe spatio-temporal magnetic field correlations that would otherwise be discarded by ensemble or sequential averaging [42]. Another application using the SPAD array would be to investigate charge transport over larger ensembles of individual NV centers, and to time correlate such dynamics [32]. It may also be possible to improve the sensing performance of the array by controlling environmental dark spins nearby individual NV centers as we do for the environmental spins X_1, X_2, and Y. In this way, the work presented in this thesis to extend the electronic-spin register around a single central NV will lay the foundation for constructing an array of hybrid NV and dark spin registers.

Appendix A

A.1 Data Analysis

We fit the individual SEDOR-ESR peaks in Figures 3-2 and 3-5 to a Lorentzian function with four free parameters:

$$f(x) = b_0 + A_0 \cdot \frac{(\frac{\gamma}{2})^2}{(x-\omega_0)^2 + (\frac{\gamma}{2})^2}, \tag{A.1}$$

from which we find $\omega_0^{X1^\downarrow} = 2\pi \cdot 41.6(4)$ MHz, $\omega_0^{X1^\uparrow} = 2\pi \cdot 68.1(4)$ MHz, $\omega_0^{X2^\downarrow} = 2\pi \cdot 53.3(3)$ MHz, $\omega_0^{X2^\uparrow} = 2\pi \cdot 56.3(4)$ MHz, $\omega_0^{Y^\downarrow} = 2\pi \cdot 44.0(2)$ MHz, and $\omega_0^{Y^\uparrow} = 2\pi \cdot 77.5(2)$ MHz. The error is taken as $\gamma/2$ (half of the FWHM).

We fit the SEDOR-Ramsey signals in Figures 3-3 and 3-6 to the following decaying cosine function:

$$f(t) = \frac{1}{2}\left(1 + \cos(2\pi d_0 t)\right) e^{-t/\tau_0}, \tag{A.2}$$

where for SEDOR-Ramsey(NV, X) we fix d_0 to the dominant frequency in its FFT spectrum, and for SEDOR-Ramsey(X, Y) both d_0 and τ_0 are free parameters.

The spin-echo decay signal in Figure 3-3 is fit to the following exponential decay function with three free parameters:

$$f(t) = b_0 + A_0 \cdot e^{-t/T_2}. \tag{A.3}$$

The Fast Fourier Transform (FFT) spectra in Figures 3-3, 3-6, 4-1, and 4-2 are

computed using the periodogram method to return the normalized power spectral density. The dominant frequency in the spectra are found by fitting the dominant peak to a Lorentzian function of the form:

$$f(x) = \frac{(\Delta d)^2}{(x - d_0)^2 + (\Delta d)^2}, \tag{A.4}$$

and the uncertainty reported for extracted dominant frequency d_0 is Δd.

The SEDOR-Ramsey decay signal for X_2 shown in Figure 3-9 is fit to the following exponential decay function with three free parameters:

$$f(t) = b_0 + A_0 \cdot e^{-(t/\tau_0)^3}. \tag{A.5}$$

The fit for the HHCP(NV,X) signal in Figure 4-1 is a decaying cosine function:

$$f(t) = b_0 + A_0 \cos(2\pi d_0 t) e^{-t/\tau_0}, \tag{A.6}$$

where b_0, A_0, and τ_0 are free parameters and d_0 is fixed to the dominant frequency in its FFT spectrum.

The fit for the HHCP(X,Y) signal in Figure 4-2, the Rabi(Y) signal in Figure 4-3, and the nuclear spin Rabi signals in Figure 3-12 is a cosine function with three free parameters:

$$f(t) = b_0 + A_0 \cdot \cos(2\pi d_0 t), \tag{A.7}$$

and the baseline subtraction to the HHCP(X, Y) data is equal to $b_0 + A_0 - 1$ such that $\langle \sigma_z^X (t = 0\ \mu s) \rangle^{\mathrm{FIT}} = 1$.

For the polarization decay curve in Figure 4-4 we fit to Equation (A.3) with b_0 fixed to equal zero. The fits in Figures 4-3 and 4-4 exclude points less than 300 ns due to a hardware issue for sequences of variable time.

Bibliography

[1] M. H. Abobeih, J. Cramer, M. A. Bakker, N. Kalb, M. Markham, D. J. Twitchen, and T. H. Taminiau. One-second coherence for a single electron spin coupled to a multi-qubit nuclear-spin environment. *Nat. Commun.*, 9:2552, 2018.

[2] M. K. Atumi, J. P. Goss, P. R. Briddon, F. E. Shrif, and M. J. Rayson. Hyperfine interactions at nitrogen interstitial defects in diamond. *J. Phys.: Condens. Matter*, 25:065802, 2013.

[3] D. D. Awschalom, R. Hanson, J. Wrachtrup, and B. B. Zhou. Quantum technologies with optically interfaced solid-state spins. *Nat. Photon.*, 12:516, 2018.

[4] G. Balasubramanian, P. Neumann, D.l Twitchen, M. Markham, R. Kolesov, N. Mizuochi, J. Isoya, J. Achard, J. Beck, J. Tissler, V. Jacques, P. R. Hemmer, F. Jelezko, and J. Wrachtrup. Ultralong spin coherence time in isotopically engineered diamond. *Nat. Mater.*, 8:383, 2009.

[5] H. P. Bartling, M. H. Abobeih, B. Pingault, M. J. Degen, S. J. H. Loenen, C. E. Bradley, J. Randall, M. Markham, D. J. Twitchen, and T. H. Taminiau. Entanglement of spin-pair qubits with intrinsic dephasing times exceeding a minute. *Phys. Rev. X*, 12:011048, 2022.

[6] J. J. Bollinger, W. M. Itano, D. J. Wineland, and D. J. Heinzen. Optimal frequency measurements with maximally correlated states. *Phys. Rev. A*, 54:R4649, 1996.

[7] C. E. Bradley, J. Randall, M. H. Abobeih, R. C. Berrevoets, M. J. Degen, M. A. Bakker, M. Markham, D. J. Twitchen, and T. H. Taminiau. A ten-qubit solid-state spin register with quantum memory up to one minute. *Phys. Rev. X*, 9:031045, 2019.

[8] B.L. Cann. *Magnetic resonance studies of point defects in diamond*. PhD thesis, University of Warwick, 2009.

[9] F. Casola, T. van der Sar, and A. Yacoby. Probing condensed matter physics with magnetometry based on nitrogen-vacancy centres in diamond. *Nat. Rev. Mater.*, 3:17088, 2018.

[10] A. Cooper, W. K. C. Sun, J.C. Jaskula, and P. Cappellaro. Environment-assisted quantum-enhanced sensing with electronic spins in diamond. *Phys. Rev. Appl.*, 12:044047, 2019.

[11] A. Cooper, W. K. C. Sun, J.C. Jaskula, and P. Cappellaro. Identification and control of electron-nuclear spin defects in diamond. *Phys. Rev. Lett.*, 124:083602, 2020.

[12] E. J. Davis, B. Ye, F. Machado, S. A. Meynell, W. Wu, T. Mittiga, W. Schenken, M. Joos, B. Kobrin, Y. Lyu, Z. Wang, D. Bluvstein, S. Choi, C. Zu, A. C. Bleszynski Jayich, and N. Y. Yao. Probing many-body dynamics in a two-dimensional dipolar spin ensemble. *Nat. Phys.*, 19:836, 2023.

[13] G. de Lange, T. van der Sar, M. Blok, Z.H. Wang, V. Dobrovitski, and R. Hanson. Controlling the quantum dynamics of a mesoscopic spin bath in diamond. *Sci. Rep.*, 2:382, 2012.

[14] C. L. Degen, F. Reinhard, and P. Cappellaro. Quantum sensing. *Rev. Mod. Phys.*, 89:035002, 2017.

[15] M. J. Degen, S. J. H. Loenen, H. P. Bartling, C. E. Bradley, A. L. Meinsma, M. Markham, D. J. Twitchen, and T. H. Taminiau. Entanglement of dark electron-nuclear spin defects in diamond. *Nat. Commun.*, 12:3470, 2021.

[16] D.P. DiVincenzo. The physical implementation of quantum computation. *Fortschritte Phys.*, 48:771, 2000.

[17] F. Dolde, V. Bergholm, Y. Wang, I. Jakobi, B. Naydenov, S. Pezzagna, J. Meijer, F. Jelezko, P. Neumann, T. Schulte-Herbrüggen, J. Biamonte, and J. Wrachtrup. High-fidelity spin entanglement using optimal control. *Nat. Commun.*, 5:3371, 2014.

[18] B. L. Dwyer, L. V. H. Rodgers, E. K. Urbach, D. Bluvstein, S. Sangtawesin, H. Zhou, Y. Nassab, M. Fitzpatrick, Z. Yuan, K. De Greve, E. L. Peterson, H. Knowles, T. Sumarac, J. P. Chou, A. Gali, V. V. Dobrovitski, M. D. Lukin, and N. P. de Leon. Probing spin dynamics on diamond surfaces using a single quantum sensor. *PRX Quantum*, 3:040328, 2022.

[19] K. M. Etmimi, M. E. Ahmed, P. R. Briddon, J. P. Goss, and A. M. Gsiea. Nitrogen-pair paramagnetic defects in diamond: A density functional study. *Phys. Rev. B*, 79:205207, 2009.

[20] G. Goldstein, P. Cappellaro, J. R. Maze, J. S. Hodges, L. Jiang, A. S. Sørensen, and M. D. Lukin. Environment-assisted precision measurement. *Phys. Rev. Lett.*, 106:140502, 2011.

[21] S. R. Hartmann and E. L. Hahn. Nuclear double resonance in the rotating frame. *Phys. Rev.*, 128:2042, 1962.

[22] S. F. Huelga, C. Macchiavello, T. Pellizzari, A. K. Ekert, M. B. Plenio, and J. I. Cirac. Improvement of frequency standards with quantum entanglement. *Phys. Rev. Lett.*, 79:3865, 1997.

[23] I. G. Hughes and T. P. A. Hase. *Measurements and their Uncertainties*. Oxford University Press, 2010.

[24] K. Iakoubovskii and G. J. Adriaenssens. Optical transitions at the substitutional nitrogen centre in diamond. *J. Phys.: Condens. Matter*, 12:L77, 2000.

[25] K. Iakoubovskii and A. Stesmans. Characterization of hydrogen and silicon-related defects in cvd diamond by electron spin resonance. *Phys. Rev. B*, 66:195207, 2002.

[26] I. Jakobi, S. A. Momenzadeh, F. F. de Oliveira, J. Michl, F. Ziem, M. Schreck, P. Neumann, A. Denisenko, and J. Wrachtrup. Efficient creation of dipolar coupled nitrogen-vacancy spin qubits in diamond. *J. Phys.: Conf. Ser.*, 752:012001, 2016.

[27] J. C. Jaskula, E. Bauch, S. Arroyo-Camejo, M. D. Lukin, S. W. Hell, A. S. Trifonov, and R. L. Walsworth. Superresolution optical magnetic imaging and spectroscopy using individual electronic spins in diamond. *Opt. Express*, 25:11048, 2017.

[28] L. Jiang, J. S. Hodges, J. R. Maze, P. Maurer, J. M. Taylor, D. G. Cory, P. R. Hemmer, R. L. Walsworth, A. Yacoby, A. S. Zibrov, and M. D. Lukin. Repetitive readout of a single electronic spin via quantum logic with nuclear spin ancillae. *Science*, 326:267, 2009.

[29] H.S. Knowles, D.M. Kara, and M. Atatüre. Demonstration of a coherent electronic spin cluster in diamond. *Phys. Rev. Lett.*, 117:100802, 2016.

[30] J. Lee, M. Tatsuta, A. Xu, E. Bauch, M. J. H. Ku, and R. L. Walsworth. Dressed-state control of effective dipolar interaction between strongly-coupled solid-state spins. arXiv:2203.07610 [quant-ph], 2023.

[31] A. Lourette, S.and Jarmola, V. M. Acosta, A. G. Birdwell, D. Budker, M. W. Doherty, T. Ivanov, and V. S. Malinovsky. Temperature sensitivity of ^{14}n-v and ^{15}n-v ground-state manifolds. *Phys. Rev. Appl.*, 19:064084, 2023.

[32] A. Lozovoi, H. Jayakumar, D. Daw, G. Vizkelethy, B. Edward, M. W. Doherty, J. Flick, and C. A. Meriles. Optical activation and detection of charge transport between individual colour centres in diamond. *Nat. Electron*, 4:717, 2021.

[33] M. Mehring and J. Mende. Spin-bus concept of spin quantum computing. *Phys. Rev. A*, 73:052303, 2006.

[34] T.A. Mittiga. *Sensing the local charge and strain environments surrounding Nitrogen-Vacancy centers in diamond.* PhD thesis, University of California, Berkeley, 2020.

[35] M.J. Munro, K. Azuma, K. Tamaki, and K. Nemoto. Inside quantum repeaters. *IEEE J. Sel. Top.*, 21:78, 2015.

[36] B. Naydenov, F. Reinhard, A. Lämmle, V. Richter, R. Kalish, U. F. S. D'Haenens-Johansson, M. Newton, F. Jelezko, and J. Wrachtrup. Increasing the coherence time of single electron spins in diamond by high temperature annealing. *Appl. Phys. Lett.*, 97:242511, 2010.

[37] P. Neumann. *Towards a room temperature solid state quantum processor — The nitrogen-vacancy center in diamond.* PhD thesis, University of Stuttgart, 2011.

[38] P. Neumann, J. Beck, M. Steiner, F. Rempp, H. Fedder, P. R. Hemmer, J. Wrachtrup, and F. Jelezko. Single-shot readout of a single nuclear spin. *Science*, 329:542, 2010.

[39] C. V. Peaker. *First principles study of point defects in diamond.* PhD thesis, Newcastle University, 2018.

[40] J. Randall, C. E. Bradley, F. V. van der Gronden, A. Galicia, M. H. Abobeih, M. Markham, D. J. Twitchen, F. Machado, N. Y. Yao, and T. H. Taminiau. Many-body–localized discrete time crystal with a programmable spin-based quantum simulator. *Science*, 374:1474, 2021.

[41] E. L. Rosenfeld, L. M. Pham, M. D. Lukin, and R. L. Walsworth. Sensing coherent dynamics of electronic spin clusters in solids. *Phys. Rev. Lett.*, 120:243604, 2018.

[42] J. Rovny, Z. Yuan, M. Fitzpatrick, A. I. Abdalla, L. Futamura, C. Fox, M. C. Cambria, S. Kolkowitz, and N. P. de Leon. Nanoscale covariance magnetometry with diamond quantum sensors. *Science*, 378:1301, 2022.

[43] M. Schaffry, E. M. Gauger, J. J. L. Morton, and S. C. Benjamin. Proposed spin amplification for magnetic sensors employing crystal defects. *Phys. Rev. Lett.*, 107:207210, 2011.

[44] L. Schlipf, T. Oeckinghaus, K. Xu, D. Dasari, Bhaktavatsala R., A. Zappe, F. F. de Oliveira, B. Kern, M. Azarkh, M. Drescher, M. Ternes, K. Kern, J. Wrachtrup, and A. Finkler. A molecular quantum spin network controlled by a single qubit. *Sci. Adv.*, 3:e1701116, 2017.

[45] A. Schweiger and G. Jeschke. *Principles of Pulse Electron Paramagnetic Resonance.* Oxford University Press, 2001.

[46] A. Sipahigil, R. E. Evans, D. D. Sukachev, M. J. Burek, J. Borregaard, M. K. Bhaskar, C. T. Nguyen, J. L. Pacheco, H. A. Atikian, C. Meuwly, R. M. Camacho, F. Jelezko, E. Bielejec, H. Park, M. Lončar, and M. D. Lukin. Loophole-free bell inequality violation using electron spins separated by 1.3 kilometres. *Science*, 354:847, 2016.

[47] W. K. C. Sun. *Developing Small-scale Quantum Information Processors based on Electronic Spins in Diamond*. PhD thesis, Massachusetts Institute of Technology, 2021.

[48] W. K. C. Sun and P. Cappellaro. Self-consistent noise characterization of quantum devices. *Phys. Rev. B*, 106:155413, 2022.

[49] A. O. Sushkov, I. Lovchinsky, N. Chisholm, R. L. Walsworth, H. Park, and M. D. Lukin. Magnetic resonance detection of individual proton spins using quantum reporters. *Phys. Rev. Lett.*, 113:197601, 2014.

[50] P. Szańkowski, M. Trippenbach, and L. Cywiński. Spectroscopy of cross correlations of environmental noises with two qubits. *Phys. Rev. A*, 94:012109, 2016.

[51] T. H. Taminiau, J. Cramer, T. van der Sar, V. V. Dobrovitski, and R. Hanson. Universal control and error correction in multi-qubit spin registers in diamond. *Nat. Nanotech.*, 9:171, 2014.

[52] J. P. Tetienne, L. Rondin, P. Spinicelli, M. Chipaux, T. Debuisschert, J. F. Roch, and V. Jacques. Magnetic-field-dependent photodynamics of single nv defects in diamond: an application to qualitative all-optical magnetic imaging. *New J. Phys*, 14:103033, 2012.

[53] A. Ungar, P. Cappellaro, A. Cooper, and W. K. C Sun. Identification and control of an environmental spin defect beyond the coherence limit of a central spin. arXiv:2306.17155 [quant-ph], 2023.

[54] U. von Lüpke, F. Beaudoin, L. M. Norris, Y. Sung, R. Winik, J. Y. Qiu, M. Kjaergaard, D. Kim, J. Yoder, S. Gustavsson, L. Viola, and W. D. Oliver. Two-qubit spectroscopy of spatiotemporally correlated quantum noise in superconducting qubits. *PRX Quantum*, 1:010305, 2020.

[55] G. Wang, F. Madonini, B. Li, C. Li, J. Xiang, F. Villa, and P. Cappellaro. Fast wide-field quantum sensor based on solid-state spins integrated with a spad array. *Adv Quantum Technol.*, page 2300046, 2023.

[56] B. R. Weil and J. A. Bolton. *Electron Paramagnetic Resonance: Elementary Theory and Practical Applications*. John Wiley & Sons, Inc, 2007.

[57] C. D. Wilen, S. Abdullah, N. A. Kurinsky, C. Stanford, L. Cardani, G. D'Imperio, C. Tomei, L. Faoro, L. B. Ioffe, C. H. Liu, A. Opremcak, B. G. Christensen, J. L. DuBois, and R. McDermott. Correlated charge noise and relaxation errors in superconducting qubits. *Nature*, 594:369, 2021.

[58] X. Zhou, G. D. Watkins, K.M. McNamara Rutledge, R. P. Messmer, and S. Chawla. Hydrogen-related defects in polycrystalline cvd diamond. *Phys. Rev. B*, 54:7881, 1996.